

ORSAY
n° d'ordre :

LAL 09-218
Décembre 2009

Mémoire d'Habilitation à Diriger des Recherches

Measuring Supersymmetry

Dirk ZERWAS

Habilitation soutenue le 11 Décembre 2009 devant la commission d'examen

MME.	S.	DAWSON	rapporteur
M.	K.	DESCH	rapporteur
	D.	FOURNIER	
	H.	OBERLACK	rapporteur
	J.	ORLOFF	
	G.	WORMSER	

Abstract

Supersymmetry is an attractive extension of the standard model of particle physics. It associates to every bosonic degree of freedom a fermionic one and vice versa. Supersymmetry unifies the coupling constants of the electromagnetic, weak and strong forces at a high scale and provides a candidate for the elusive dark matter. Supersymmetry could be discovered at the LHC, the proton–proton collider at CERN which has started operations in 2008. The LHC is foreseen to have a center–of–mass energy of 14 TeV, opening up a new mass range to be explored to search for supersymmetric particles with the ATLAS and CMS experiments. The development and production of electronics for these detectors has been a challenge, e.g. for the readout board for the electromagnetic calorimeter. Reconstructing the physics events with the best precision, in particular the reconstruction and identification of electrons and photons in the large QCD background has been prepared in extensive test beam studies and Monte Carlo simulations. If the Higgs boson and supersymmetry are discovered, the properties of the (s)particles such as the masses, branching ratios must be measured precisely, either at the LHC or at a future e^+e^- linear collider. The SFitter project aims to determine the underlying theoretical model parameters from the correlated experimental measurements including theoretical errors. The methods are applied to the extraction of the fundamental parameters of supersymmetry as well the measurement of the Higgs boson couplings at the LHC. The extrapolation of the supersymmetric parameters from the weak scale to the Grand Unification Scale could provide the basis towards the inclusion of gravity.

*Therefore, since brevity is the soul of wit,
And tediousness the limbs and outward flourishes,
I will be brief.*

Hamlet, Act 2 Scene 2, William Shakespeare

Contents

1	Introduction	3
2	Phenomenology of Supersymmetry	9
2.1	Supersymmetry	10
2.2	The Minimal Supersymmetric Extension of the Standard Model	12
2.3	Minimal Supergravity	15
2.4	Benchmark points	16
3	Colliders and Experiments	19
3.1	LHC	19
3.2	The ATLAS Detector	22
3.2.1	Electromagnetic Test beam	25
3.2.2	The Front End Board of the LAr Calorimeters	27
3.3	Performance of the ATLAS Detector	30
3.3.1	Electron and Photon Reconstruction	32
3.4	e^+e^- Linear Collider	35
4	Determination of Supersymmetric Parameters and Higgs Couplings	39
4.1	Low Mass Higgs Boson Signatures	40
4.2	Supersymmetric Observables for a specific Parameter Set	45
4.3	Treatment of Errors	48
4.4	Measuring mSUGRA	50
4.4.1	Determination of the True Central Value	50
4.4.2	Determining the Errors on the Parameters	52
4.5	Measuring the MSSM	54
4.5.1	Determination of the True Central Value	56
4.5.2	Determining the Errors	56

4.5.3	Extrapolating to the GUT Scale	57
4.6	Measuring the Higgs Sector	60
4.6.1	Determination of the True Couplings	61
4.6.2	Error determination	63
4.6.3	Supersymmetric Higgs Scenarios	65
5	Conclusions	67

Chapter 1

Introduction

The Standard Model of elementary particle physics [1, 2, 3] describes matter and its interactions with an unprecedented degree of precision. Matter is built of fermions (quarks and leptons) and their interactions are mediated via bosons. The photon (γ) is responsible for the electromagnetic interactions, the charged vector bosons (W^\pm) and the Z boson are the carriers of the weak force. The gluons mediate the strong interaction. Masses are generated via the Higgs mechanism, leading to an additional neutral scalar particle, the Higgs boson (H) [4, 5, 6, 7, 8].

Supersymmetry is the next logical step after gauge theories [9]. In supersymmetric theories a fermionic degree of freedom is associated to every bosonic degree of freedom and vice-versa [10, 11, 12, 13, 14] (and references therein). Ultra-violet completions of the Standard Model lead to quantum corrections on the Higgs boson mass of the order of the new physics scale, larger than the Higgs boson itself, whereas in supersymmetry these large corrections cancel. Supersymmetry can solve this hierarchy problem in a natural way. In the Standard Model the coupling constants of the strong, weak and electromagnetic interactions, extrapolated via renormalization group equations (RGEs), do not meet in one point. Supersymmetry modifies this behavior to unify the constants at about 10^{16} GeV (grand unification scale, GUT scale) [15, 16, 17]. Additionally supersymmetry is attractive as it provides a candidate for the elusive dark matter.

To construct supersymmetric models such as the minimal supersymmetric extension of the Standard Model (MSSM) or minimal Supergravity (mSUGRA), the Higgs sector has to be extended to give masses to up and down type quarks. The two Higgs doublets are necessary: to avoid anomalies

and large flavor changing neutral currents (FCNC). In the Standard Model the Higgs field and its complex conjugate field are used to give masses to up and down type quarks, while in a supersymmetric theory the complex conjugate field cannot be used, necessitating the second doublet. The Higgs sector of the MSSM contains five Higgs bosons: h , H , A and H^\pm . The lightest Higgs boson must be light with a mass of less than $140 \text{ GeV}/c^2$. Additionally the sfermions, the partners of the fermions, are predicted. The supersymmetric partners of the neutral gauge and Higgs bosons mix to form the neutralinos. The charginos are mixtures of the supersymmetric partners of the charged Higgs and gauge bosons.

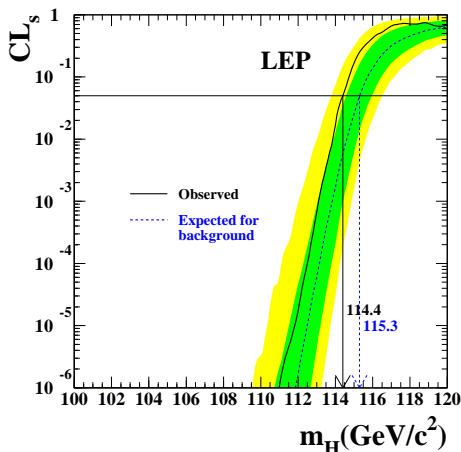


Figure 1.1: The expected and observed lower limit on the Standard Model Higgs boson mass obtained by the LEP collaborations is shown [18].

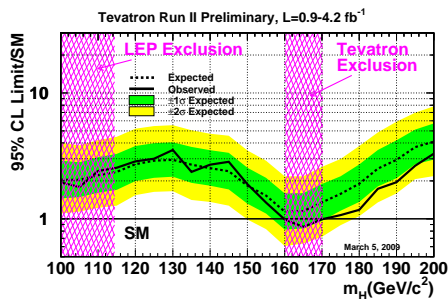


Figure 1.2: The expected and observed lower limit on the Standard Model Higgs boson mass obtained by the CDF and Do collaborations is shown [19].

The most precise measurements of parameters of the Standard Model are obtained from e^+e^- colliders such as LEP and SLC, as well as the proton-antiproton ($p\bar{p}$) collider TeVatron at Fermilab. ALEPH, DELPHI, L3 and OPAL took data from 1989 to 2000 at LEP, operating at center-of-mass energies from 91 GeV to 209 GeV. The SLD detector operated at SLAC's e^+e^- SLC at a center-of-mass energy of about 91 GeV. CDF and D0 are taking data at the TeVatron, operating at a center-of-mass energy of 1.96 TeV. In 2009 the proton-proton (pp) collider LHC at CERN will effectively start

operations. The center-of-mass energy is foreseen to be 7 TeV which will be increased to 14 TeV in the coming years. ATLAS and CMS are the two multi-purpose detectors located at the LHC. They are optimized for the search of the Higgs boson(s) and new physics. The e^+e^- Linear Collider project (ILC) is being prepared for a center-of-mass energy from 500 GeV to 1 TeV. A decision on whether the ILC will be built is expected after the analysis of the first LHC data. R&D is being performed for a linear collider (CLIC) which may be capable of running at 3 TeV.

The search for the Standard Model Higgs boson at LEP has led to a limit of $114.4 \text{ GeV}/c^2$ [18] as shown in Figure 1.1, slightly smaller than the expected limit of $115.3 \text{ GeV}/c^2$. Time will tell whether the events observed at LEP around this mass will turn out to have been the first indication of the Higgs boson or not.

The TeVatron is particularly sensitive to the Standard Model Higgs boson for masses of the order 150-180 GeV/c^2 . In this mass region the decay of the Higgs boson to a pair of W^\pm bosons is dominant. The combination of several channels from both CDF and D0 has led to the first new limit beyond the LEP bound: a Standard Model Higgs boson with a mass of 160 to 170 GeV/c^2 is excluded at 95% confidence level [19, 20] as shown in Figure 1.2.

The precise measurement of the electroweak parameters at LEP and SLC are discussed in detail in [21]. The most precise individual measurements of the W^\pm boson mass are from CDF [22] and D0 [23] which have reached a precision of $48 \text{ MeV}/c^2$ and $43 \text{ MeV}/c^2$ respectively. The combination of all W^\pm mass measurements leads to $80.399 \pm 0.023 \text{ GeV}/c^2$. The top quark mass has now been measured with a precision better than percent as shown in [24]. The predictions of the electroweak observables depend via quantum corrections on the mass of the Higgs boson, especially the W^\pm boson and top quark masses. Their sensitivity is illustrated in Figure 1.4 where the solid line denotes the experimental measurements of the W^\pm boson and top quark masses and the straight lines different Higgs boson mass hypotheses. Combining all measurements in a fit the Higgs boson mass can be determined to be $84_{-26}^{+34} \text{ GeV}/c^2$. This leads to an upper limit of $157 \text{ GeV}/c^2$ on the Higgs boson mass at 95% confidence level. Thus the data prefer a light Higgs boson mass.

In addition to the Standard Model production mode, albeit with modified couplings, the associated production of Higgs bosons, such as the h produced in association with the A , can also be used in the search for the MSSM Higgs bosons. Limits on neutral MSSM Higgs bosons have been determined to be

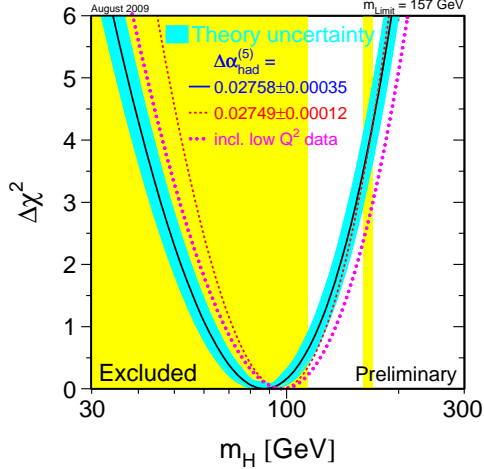


Figure 1.3: The result of the electroweak fit is shown as function of the Higgs boson mass. The yellow shaded area shows the region excluded by the direct search.

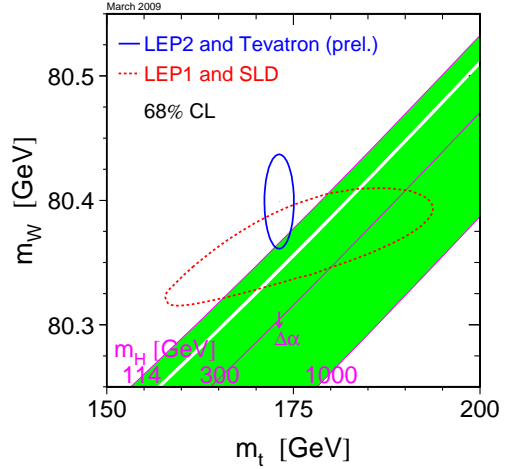


Figure 1.4: The measurement of the W^\pm boson mass as function of the top quark mass is shown (solid line). The dotted line shows the indirect constraints on the W^\pm boson mass and top quark mass. The straight lines show different Higgs mass hypotheses (update of [21]).

be $92.8 \text{ GeV}/c^2$ for the h and $93.4 \text{ GeV}/c^2$ for the A boson [25]. The searches for the neutral MSSM Higgs bosons can also be interpreted as limit on the ratio of the vacuum expectation values (vevs) of the two Higgs doublets $\tan \beta$. $\tan \beta$ between 0.7 and 2 are excluded as shown in Figure 1.5. Some variation of the excluded region is possible as it depends on the top quark mass and the parameters of the supersymmetric model.

As the cross section for the pair production of scalars is proportional to β^3 , where $\beta = \sqrt{1 - 4m_{H^\pm}^2/s}$, the mass limit on the charged Higgs bosons from the combination of the LEP experiments has not reached the kinematic limit. Charged Higgs boson masses of less than $78.6 \text{ GeV}/c^2$ are excluded at 95% confidence level [26].

LEP has set mass limits on selectrons and muons (cross section $\sim \beta^3$) at $95 \text{ GeV}/c^2$ and slightly weaker limits on the stau slepton of $87 \text{ GeV}/c^2$ [27]. Charginos with masses of up to $103 \text{ GeV}/c^2$ (cross section $\sim \beta$), i.e. es-

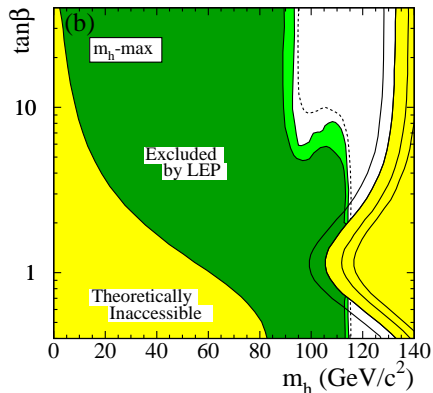


Figure 1.5: The region excluded by LEP and by theory in the plane $\tan\beta$ versus mass of the lightest Higgs boson [25].

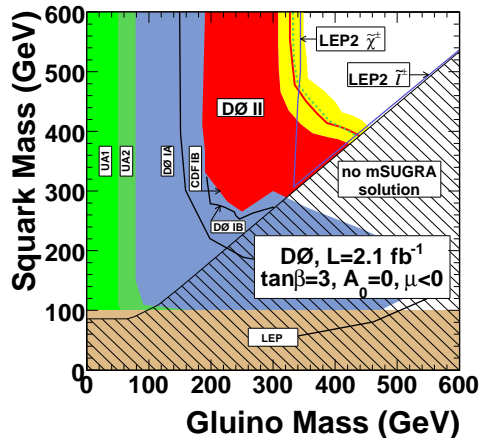


Figure 1.6: The regions excluded by the TeVatron and LEP in the plane of the squark mass versus the gluino mass are shown [30].

essentially up to the kinematic limit, have been excluded [28]. Combining all searches a lower limit on the mass of the lightest neutralino of $50 \text{ GeV}/c^2$ has been obtained in mSUGRA [29].

The TeVatron is on the forefront of the search for supersymmetric colored particles, the squarks and gluinos. In the absence of a signal, lower limits on the mass of the sparticles have been set. These depend on the specific scenario chosen. As an example, for a given typical choice of parameters, squarks of mass less than $392 \text{ GeV}/c^2$ have been excluded and a limit of $327 \text{ GeV}/c^2$ on the mass of the gluino has been obtained. For equal squark and gluino masses a lower limit of $408 \text{ GeV}/c^2$ has been determined [30] (and references therein) as shown in Figure 1.6.

Several aspects of the search for supersymmetry and its measurement will be discussed in the following. In chapter 2, the phenomenology of the most important supersymmetric models will be reviewed. Chapter 3 contains a brief discussion of experimental aspects of the search for supersymmetry. In particular a part of the Front End Electronics of the ATLAS electromagnetic calorimeter as well as the performance of the reconstruction of electrons and photons are described in more detail, based on Refs. [31, 32, 33]. In chapter 4 the determination of supersymmetric parameters from experimental

measurements as well as the determination of the Higgs boson couplings at the LHC will be discussed. The results summarized in this chapter are explained in more detail in Refs. [34, 35, 36]. In the last chapter the results will be summarized and an outlook for the future will be given.

Chapter 2

Phenomenology of Supersymmetry

To construct a supersymmetric extension of the Standard Model, such as the MSSM and mSUGRA, an extended Higgs sector is necessary in order to give masses to up and down type quarks as well as the addition of partners of the standard model particle. Further extensions, such as the MSSM with an additional singlet (NMSSM), have an even richer spectrum of Higgs bosons and possibly new signatures with respect to the MSSM [37]. In this chapter the discussion is restricted to the MSSM and mSUGRA. The parameters of the MSSM are defined at the electroweak scale, whereas the parameters of mSUGRA are defined at the GUT scale. R-parity will be conserved in the following, therefore supersymmetric particles are produced in pairs, (cascade-) decaying to the lightest supersymmetric particle (LSP). The LSP is stable, neutral and weakly interacting, leading to the characteristic signature for supersymmetry at a collider, missing energy.

The slope of the gauge couplings' running is modified at a scale of about 1 TeV by Supersymmetry, leading to a unification of the couplings at about 10^{16} GeV. As this scale is close to the Planck scale (10^{18} GeV), Supersymmetry could be a telescope to physics at this scale. A side effect of this unification at a higher scale compared to the Standard Model is that the proton can have a longer lifetime.

The Standard Model accounts for only 4% of the energy of the universe. 24% are due to dark matter. The LSP of supersymmetry is prime candidate for dark matter as it is neutral and weakly interacting.

From an experimental point of view it is intriguing to note that the Stan-

Standard Model electroweak fits favor a light Higgs boson with a mass less than $157 \text{ GeV}/c^2$. Supersymmetry, as realized in the MSSM, predicts a lightest Higgs boson which should have a mass less than about $140 \text{ GeV}/c^2$.

Ultra-violet completions of the Standard Model lead to quantum corrections on the mass of the Higgs boson of the order of this new physics scale. This unnatural behavior is corrected in supersymmetry where an equal number of fermions and bosons leads to a cancellation of the corrections. In order to preserve the natural cancellation in the Higgs sector the breaking of Supersymmetry, i.e. lifting the mass degeneracy of standard and supersymmetric particles, cannot be arbitrarily large, but must be at most of the order of TeV.

These arguments motivate the search for Supersymmetry. In the following sections a few basic considerations of supersymmetry and the phenomenology of two models, the MSSM and mSUGRA, will be discussed.

2.1 Supersymmetry

Supersymmetry was presented first in [10, 11, 12]. The construction of viable models was pioneered by Fayet and Iliopoulos [13]

At the Planck scale $M_{\text{P}} = 2.4 \cdot 10^{18} \text{ GeV}/c^2$, gravitational effects are important. The corrections to the Higgs boson mass in the Standard Model would have to be fine-tuned to one part in 10^{16} to give a Higgs mass of the order of the electroweak scale if the Standard Model were to be valid up to this scale. As supersymmetric models contain two scalars for every fermion, the quadratic divergences cancel and only the logarithmic parts remain. The fermion masses, including radiative corrections, are logarithmically divergent. Including additionally soft supersymmetry breaking, qualitatively the corrections to the Higgs boson mass then take on the following form (m_{soft} is the mass splitting between the fermion and the scalars) [14]:

$$\Delta m_{\text{H}}^2 = m_{\text{soft}}^2 \left[\frac{\lambda}{16\pi^2} \ln(\Lambda/m_{\text{soft}}) + \dots \right] \quad (2.1)$$

If $\lambda \sim 1$ and Λ the Planck scale, for a soft supersymmetry breaking mass of $1 \text{ TeV}/c^2$, the correction to the Higgs boson mass will be about $500 \text{ GeV}/c^2$. Since the correction increases about linearly with m_{soft} , therefore the masses of at least some of the supersymmetric particles must be less than about $1 \text{ TeV}/c^2$.

Supersymmetry is a spacetime symmetry. The Haag-Lopuszanski-Sohnius [38] extension of the Coleman-Mandula [39] theorem restricts the forms of such symmetries in interacting quantum field theories. In practice for extensions of the Standard Model, the generators Q , Q^\dagger have to satisfy an algebra of the form [14]:

$$\begin{aligned} \{Q, Q^\dagger\} &= \sigma_\mu P^\mu \\ \{Q, Q\} &= \{Q^\dagger, Q^\dagger\} = 0 \\ [P^\mu, Q] &= [P^\mu, Q^\dagger] = 0 \end{aligned} \tag{2.2}$$

where Q generates the transformation of a fermion to a boson and vice versa, and P^μ is the momentum generator of spacetime translations. As in [14] the spinor indices have been omitted.

Supermultiplets are introduced in which a boson and a fermion must be present. Scalars and fermions are arranged in a matter (or chiral) multiplet, vector bosons and fermions are arranged in a gauge (or vector) multiplet.

Supersymmetry breaking terms, which do not reintroduce quadratic divergences, are added to the Lagrangian by hand [40] (in the notation of [14]):

$$\mathcal{L} = -\frac{1}{2}(M_\lambda \lambda^a \lambda^a + c.c.) - (m^2)_j^i \phi^{j*} \phi_i - \left(\frac{1}{2} b^{ij} \phi_i \phi_j + \frac{1}{6} a^{ijk} \phi_i \phi_j \phi_k + c.c. \right) \tag{2.3}$$

There is a gaugino mass term (M_λ) for each gauge group, scalar mass terms ($(m^2)_j^i$, b^{ij}) and a trilinear coupling a^{ijk} . These terms are added *ad hoc* to parametrize the current ignorance of the mechanism of supersymmetry breaking.

If supersymmetry is gauged locally, gravity can be incorporated, leading to supergravity. The graviton, a massless spin-2 particle, must have a supersymmetric partner (gravitino, spin- $\frac{3}{2}$). The gravitino can help solving the problem of generating the soft supersymmetry breaking masses flavor-blind where a hidden sector is introduced which communicates with the visible sector via gravitational interactions (gravitino condensation in the hidden sector). The hidden sector is connected to the gaugino and scalar soft supersymmetry breaking terms. Additional terms ensure that different soft breaking masses can be generated for each superparticle.

2.2 The Minimal Supersymmetric Extension of the Standard Model

Each Standard Model particle (or rather degree of freedom) receives a new particle as partner. The following section follows closely the notation of [14, 41]. The parameters of the MSSM are defined at the electroweak scale.

spin-0	spin-1/2	spin-1
\tilde{q}_R, \tilde{q}_L	q	
	\tilde{g}	g
$\tilde{\ell}_R, \tilde{\ell}_L$	ℓ	
	$\tilde{\gamma}$	γ
H	\tilde{H}, \tilde{Z}	Z
h A	\tilde{h}	
H^\pm	$\tilde{H}^\pm, \tilde{W}^\pm$	W^\pm

Table 2.1: The (s)particle content of the MSSM

Two Higgs doublets of opposite hypercharge are used to avoid triangle anomalies and FCNCs. Different Higgs fields give masses to the up- and down-type particles. The complete list of (s)particles and their superpartners is shown in Table 2.1.

$$\begin{aligned}
 V = & (m_1^2 + |\mu|^2)H_1^{i*}H_1^i + (m_2^2 + |\mu|^2)H_2^{i*}H_2^i - m_{12}^2(\epsilon_{ij}H_1^iH_2^j + h.c.) \\
 & + \frac{1}{8}(g^2 + g'^2)[H_1^{i*}H_1^i - H_2^{j*}H_2^j]^2 + \frac{1}{2}g^2|H_1^{i*}H_2^i|^2
 \end{aligned}
 \tag{2.4}$$

Up-type fermion masses are proportional to v_1 , the vacuum expectation value of the first doublet, and down-type fermion masses to v_2 , the vacuum expectation value of the second doublet. The parameter μ is the supersymmetric Higgs mass parameter. The parameters governing the Higgs sector are usually taken to be the mass of the lightest neutral CP-even Higgs boson (h) or CP-odd Higgs boson (A), $\tan \beta$ and m_W from the electroweak sector.

At tree level at least one Higgs boson should be lighter or as light as the Z boson. However, this stringent bound for the neutral Higgs bosons is loosened substantially by radiative corrections, which are driven mostly by

the heavy top quark mass and the top squark masses:

$$\Delta m_h^2 = \frac{3g^2}{8\pi^2} \frac{m_t^4}{m_W^2} \ln \frac{m_{\tilde{t}_1} m_{\tilde{t}_2}}{m_t^2} \quad (2.5)$$

The only strong prediction remaining after including these corrections is that the lightest neutral Higgs boson (h) must have a mass less than about 140 GeV.

In the leptonic sector each charged lepton receives two scalar partners, called L- and R-sleptons (\tilde{e}_L, \tilde{e}_R), where “L” and “R” refer to the chirality state of the corresponding lepton. For the neutrino there is one sneutrino ($\tilde{\nu}_L$). In the gauge sector the partners of the neutral gauge and Higgs bosons mix to form the neutralinos: $\chi_1^0, \chi_2^0, \chi_3^0, \chi_4^0$. In turn the partners of the charged gauge and Higgs bosons mix to form the chargino mass eigenstates χ_1^\pm and χ_2^\pm . The gluon, as a massless spin-1 particle is grouped with the gluino, its fermionic partner.

R-parité [42] is used to avoid certain yukawa terms ($\lambda_{ijk}, \lambda'_{ijk}, \lambda''_{ijk}$) which are allowed in a general supersymmetric Lagrangian, but can lead to a rapid proton decay inconsistent with experimental limits. The conservation of this multiplicative quantum number in the following studies has as consequence that supersymmetric particles must be produced in pairs. They decay, possibly via cascade decays, until the lightest supersymmetric particle is reached, which is stable.

The lightest neutralino is a good candidate for the lightest supersymmetric particle. It is color-neutral, not charged and interacts only weakly with matter. The lightest neutralino is a good candidate to solve the dark matter problem of the universe.

Certain relationships among supersymmetric particles hold:

$$m_{\tilde{t}_L}^2 = m_{\tilde{\nu}}^2 - \cos^2 \theta_W m_Z^2 \cos 2\beta \quad (2.6)$$

Consequently the left-handed slepton must always be heavier than the sneutrino, if $\tan \beta$ is greater than unity. Similar relationships hold in the squark sector.

The mass matrix for down-type squarks and charged sleptons can be written in the following way in the basis of left-handed and right-handed sfermion:

$$\begin{pmatrix} m_{\tilde{f}_L}^2 & m_f(A_{\tilde{f}} - \mu \tan \beta) \\ m_f(A_{\tilde{f}} - \mu \tan \beta) & m_{\tilde{f}_R}^2 \end{pmatrix} \quad (2.7)$$

the off-diagonal matrix elements are proportional to the trilinear coupling A_f and to the fermion's mass. Since the mixing angle is governed by the fermion mass, it is expected that in the first two generations the weak eigenstates are equal to the mass eigenstates, so the trilinear mass terms for the first two generations are usually neglected in the scalar sector. For the up-type squarks $\tan\beta$ must be replaced by $\cot\beta$.

The MSSM is governed by about 120 parameters. Not allowing CP violation, requiring the trilinear terms to be real, requiring the soft supersymmetry breaking parameters in the scalar sector to be generation-diagonal to avoid additional sources of flavor changing neutral currents, reduces the number of parameters substantially. Additionally, the trilinear mass terms of the first two generations are neglected as their impact on the mass mixing is essentially undetectable experimentally.

Another experimental requirement on the soft mass breaking terms in the first and second generation squark terms is derived from the inability to flavor tag, i.e., differentiate between u-, d-, s- and c-quarks. Adding everything together, a phenomenological MSSM is constructed. This pMSSM is governed by the following parameters in the supersymmetric sector and will be called MSSM in the following for simplicity: the Higgsino mass term (μ), the mass of the CP-odd Higgs boson mass (m_A), the ratio of the vacuum expectation values ($\tan\beta$), the gaugino mass parameters (M_1, M_2, M_3), 6 soft breaking parameters for sleptons ($M_{\tilde{e}_L}, M_{\tilde{e}_R}, M_{\tilde{\mu}_L}, M_{\tilde{\mu}_R}, M_{\tilde{\tau}_L}, M_{\tilde{\tau}_R}$), 2 soft breaking parameters for the first and second generation squarks ($M_{\tilde{q}_L}, M_{\tilde{q}_R}$), 3 soft breaking parameters for the third generation squarks ($M_{\tilde{t}_R}, M_{\tilde{b}_R}, M_{\tilde{q}_{3L}}$) and 3 trilinear parameters in the scalar fermion sector (A_τ, A_t, A_b).

In addition to the supersymmetric parameters, for a precise prediction of supersymmetric observables, the following Standard Model parameters are necessary: the electromagnetic coupling constant at the Z-mass ($\alpha(m_Z)$) the Fermi constant, the QCD coupling constant at the Z-mass (α_S), the Z-boson pole mass, mass of the bottom quark in the MSbar scheme, the pole mass of the top quark and the pole mass of the tau lepton. Thus in total $20 + 7$ parameters govern the MSSM.

The electroweak scale where the supersymmetric parameters are defined needs to be specified. It is sometimes taken to be the geometric mean of the stop quark masses. This scale would then, in some scenarios, depend on the mass of a sparticle which has not yet been measured. Therefore the proposal of the SPA project [43] is followed by fixing the scale to $1 \text{ TeV}/c^2$.

2.3 Minimal Supergravity

While the MSSM is a general model depending on few assumptions, for practical purposes it is useful to define also a restricted model, motivated by supergravity: mSUGRA. The mSUGRA parameters are mostly defined at the GUT scale. The parameters are then evolved via renormalization group equations (RGEs) to the electroweak scale at 1 TeV. Every mSUGRA parameter set has a corresponding MSSM equivalent, however not every MSSM parameter set has an mSUGRA equivalent. It is therefore interesting to study both approaches.

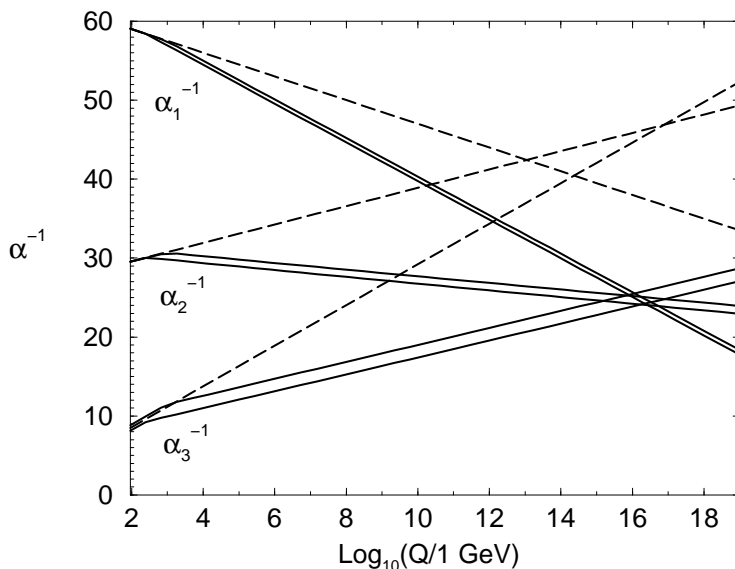


Figure 2.1: Running of α_i , $i = 1, 3$ in the Standard Model (dashed lines) and in the MSSM (full lines).

The Standard Model couplings of the three gauge groups SU(3), SU(2) and U(1), calculated according to the RGEs as a function of the mass scale, do not intersect in one point, as shown in Figure 2.1 ($\alpha_a^{-1} = g_a^2/(4\pi)$). In the MSSM [17] supersymmetric particles introduce an intermediate scale, modifying the slope after passing the threshold. In Figure 2.1 (taken from [14]), the three couplings intersect at the GUT scale ($M_U \approx 10^{16}$ GeV). Inspired by flavor neutral gravity, it is assumed that the gaugino mass parameters are also equal at the GUT scale. As a consequence M_1 , M_2 and M_3 are reduced

to one parameter at the GUT scale: $m_{1/2}$. The following relationship holds at any scale:

$$\frac{M_1}{g_1^2} = \frac{M_2}{g_2^2} = \frac{M_3}{g_3^2} = \frac{m_{1/2}}{g_U^2} \quad (2.8)$$

g_U is the coupling at the unification scale, g_3^2 is related to the strong coupling constant, and the couplings g_1 , g_2 are related to the usual electroweak constants by $g_2 = g$ and $g_1 = \sqrt{5/3}g'$

Additionally one assumes that the soft supersymmetry breaking terms for the sfermions are also universal at the GUT scale (m_0). This, however, does not imply that all sfermions have equal mass at the electroweak scale. Radiative corrections for left-handed sfermions are different from right-handed sfermions, since their couplings to gauge bosons are different. The solutions of the renormalization group equations for the masses of the right-handed slepton, the left-handed slepton and the sneutrino at the electroweak scale take on the following form:

$$\begin{aligned} m_{\tilde{\ell}_R}^2 &= m_0^2 + 0.22M_2^2 - \sin^2 \theta_W m_Z^2 \cos 2\beta + m_\ell^2 \\ m_{\tilde{\ell}_L}^2 &= m_0^2 + 0.75M_2^2 - 0.5(1 - 2\sin^2 \theta_W)m_Z^2 \cos 2\beta + m_\ell^2 \\ m_{\tilde{\nu}}^2 &= m_0^2 + 0.75M_2^2 + 0.5m_Z^2 \cos 2\beta \end{aligned} \quad (2.9)$$

A universal trilinear coupling is assumed at the GUT scale and one requires that the electroweak symmetry breaking is driven by supersymmetry [44]. This determines the supersymmetric Higgs parameter μ up to its sign.

Thus in the supersymmetric sector the following parameters remain: the ratio of the Higgs vacuum expectation values defined at the electroweak scale ($\tan \beta$), the sign of μ in the Higgs sector, the universal gaugino breaking parameter ($m_{1/2}$), the universal sfermion breaking parameter (m_0) and the trilinear term (A_0). The last three parameters are defined at the GUT scale. Additionally, as before for the MSSM, the Standard Model parameters have to be specified.

2.4 Benchmark points

Given the number of parameters, supersymmetry can lead to a wealth of different signatures at colliders. To enable comparisons between experiments

	SPS1a	SPS1a'	SU3	LM1
m_0	100	70	100	60
$m_{1/2}$	250	250	300	250
$\tan\beta$	10	10	6	10
A_0	-100	-300	-300	0

Table 2.2: Summary of mSUGRA parameter sets with similar collider phenomenology. μ is positive for all cases.

and/or colliders, sets of parameters are defined to represent typical signatures. Most commonly known is the point Snowmass Points and Slopes (SPS) 1a [45] which has been studied in detail in the LHC-ILC report [46]. Points with similar phenomenology have been studied in ATLAS (SU3) and CMS (LM1 [47]). A summary of the points is shown in Table 2.4. Common to all points are relatively light supersymmetric particles, thus an early discovery at the LHC would be possible.

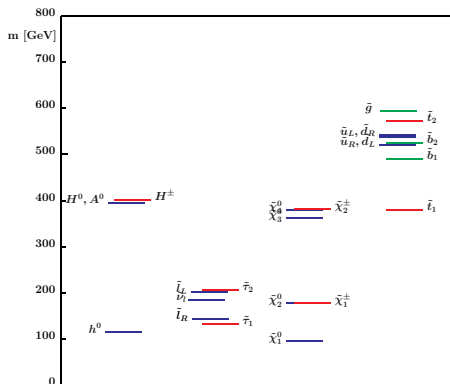


Figure 2.2: The particle spectrum of the SPS1a point is shown.

In the following SPS1a will be studied as an example. The resulting spectrum of (s)particles is shown in Figure 2.2. The parameters of this point lead to first and second generation squarks with masses of the order of 500 GeV/c². The gluino has a mass of about 600 GeV/c². The lightest right-handed sleptons have a mass of 150 GeV/c², their left-handed counter

parts have masses of $200 \text{ GeV}/c^2$. The lightest Higgs boson mass is at the edge of the LEP bound. There is a group of light neutralinos and chargino at about $200 \text{ GeV}/c^2$ and below as well as a group of heavy chargino and neutralinos. The right-handed squarks decay predominantly directly to their standard model partner and the lightest neutralino. The left-handed squarks have a long decay chain via the second lightest neutralino and a right-handed slepton open. As the lightest stau (with a left-handed component) is lighter than the second-lightest neutralino and the lightest chargino, the chargino decays with a branching ratio of almost 100% to stau and neutrino. The neutralino decay to stau and tau has a branching ratio of 90%.

Chapter 3

Colliders and Experiments

The Large Hadron Collider (LHC) at CERN has started operations on September 10, 2008. The LHC will collide proton beams with a center-of-mass energy of up to 14 TeV. Two multi-purpose detectors, ATLAS and CMS, are located on the LHC ring. The ILC, an e^+e^- collider with a center-of-mass energy of 500 GeV, extendable to 1 TeV is awaiting approval pending the results of the LHC. The ILC is expected to start operations eight years after approval.

In this chapter the LHC is briefly described. The ATLAS detector is discussed with emphasis on its performance, especially for electron and photon reconstruction. A hardware aspect of the readout of the Liquid Argon calorimeters is analyzed in more detail. The ILC and an associated detector concept is discussed last.

3.1 LHC

The LHC is described in detail in Ref. [48]. The nominal mode of operation of the LHC is to provide a luminosity of $10^{34}\text{cm}^{-2}\text{s}^{-1}$ at a center-of-mass energy of 14 TeV colliding proton beams. The bunch crossing frequency will be 40 MHz. The beams circulate in a tunnel with a circumference of 26.7 km which is connected to the CERN accelerator complex via two 2.5 km long transfer lines.

The luminosity at a collision point is described by the following formula:

$$L = \frac{N_b^2 n_b f_{\text{rev}} \gamma}{4\pi \epsilon \beta^*} F \quad (3.1)$$

where γ is the relativistic gamma factor (for protons at 7 TeV about 7000), ϵ the normalized transverse beam emittance ($3.75\mu\text{m}$), β^* the beta function at the interaction point (0.5 m), f_{rev} the revolution frequency, N_b is the number of particles per bunch (maximum $1.1 \cdot 10^{11}$) and n_b the number of bunches per beam, nominally 2808. Note that N_b enters as a square while n_b only linearly as the luminosity is defined per interaction point. Bunches are separated in the beam pipe by 7.5 m. To minimize beam collisions in the 130 m common beam pipe in the interaction regions (corresponding to about 17 unwanted collisions for each bunch of a beam), a small crossing of 150–200 μrad will be used. F is the geometrical reduction factor due to the non-zero cross angle. The size of a bunch is expected to be about 15 μm in the direction transverse to the beam axis and about 7 mm in the direction of the beam axis (z-direction).

The LHC tunnel consists of eight straight sections and eight arcs with a smaller radius, the LHC magnets are built to reach a strength of up to 9 T with 8.33 T being the nominal operating field for a beam momentum of 7 TeV/ c . A total of 1232 superconducting dipoles have been built in industry. Adding in quadrupole and other beam equipment, the LHC consists of about 4000 elements.

The dipoles are operated at a temperature of 1.9 K. This low temperature is achieved in a two stage process, first by cooling down to about 90 K with liquid Nitrogen and then cooling down to the operating temperature with super-fluid liquid Helium. The LHC has been divided into eight sectors. The cool-down of one sector to operating temperature takes about two months. The energy that will be stored in the beams will be around 362 MJ (60 kg of TNT) and an additional 600 MJ is stored in the magnet system. A fast system is able to extract the beam if necessary and dilute it before reaching an absorber.

The injection sequence of the beams is shown in Figure 3.1. The protons are first accelerated to 50 MeV/ c in a linear accelerator. In the Proton Synchrotron Booster (circular) they reach 1.4 GeV/ c before being transferred to the Proton Synchrotron (PS). In the PS the protons are accelerated to 25 GeV/ c and injected into the Super Proton Synchrotron (SPS). The protons with an energy of 450 GeV are then transferred from the SPS to the LHC. The beam is captured and accelerated by a superconducting RF system. In contrast to electron beams, the synchrotron radiation loss for protons is small $\sim (m_e/m_p)^4$. The energy gain per turn during the ramp to 7 TeV is 485 keV. The expected beam lifetime (until the luminosity has decreased to

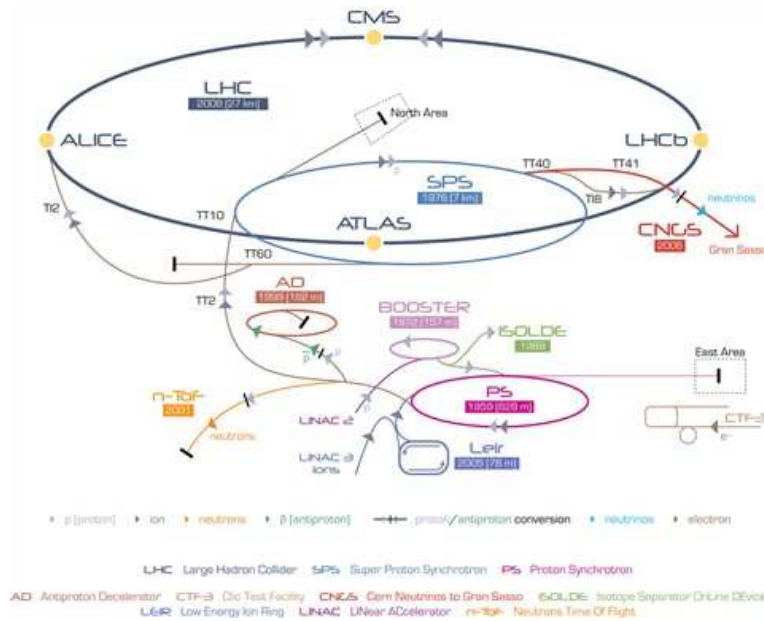


Figure 3.1: The CERN accelerator complex from the Linear accelerator to the LHC.

$1/e$) is expected to be about 15 h. The average filling time should on average be about 7 h.

The integrated luminosity per year is expected to be 10 fb^{-1} running at $10^{33} \text{ m}^{-2} \text{ s}^{-1}$. For the nominal luminosity of $10^{34} \text{ m}^{-2} \text{ s}^{-1}$, an integrated luminosity of 100 fb^{-1} is expected.

Beams were injected in both rings on September 10, 2008 and circulated many times. The RF-system has captured the beams leading to a nearly infinite theoretical lifetime. However, during the commissioning of a sector to the highest beam energy, a superconducting soldering joint turned normal conducting with a resistance of a few $\text{n}\Omega$. The small resistance was large enough to heat the super-fluid liquid helium turning it into its gaseous state. The volume expansion was so quick that the safety valves did not follow quickly enough. The shock wave displaced several magnets. About 50 elements of the machine have been repaired or replaced by spares. Additional safeguards are being put in place.

After the incident in 2008, repairs of the cryogenic as well as the magnet system are underway. The current startup plan aims to restart the machine

in November 2009 with a maximum center-of-mass energy of 7 TeV. The ramp up to the nominal center-of-mass energy of 14 TeV is foreseen for later.

3.2 The ATLAS Detector

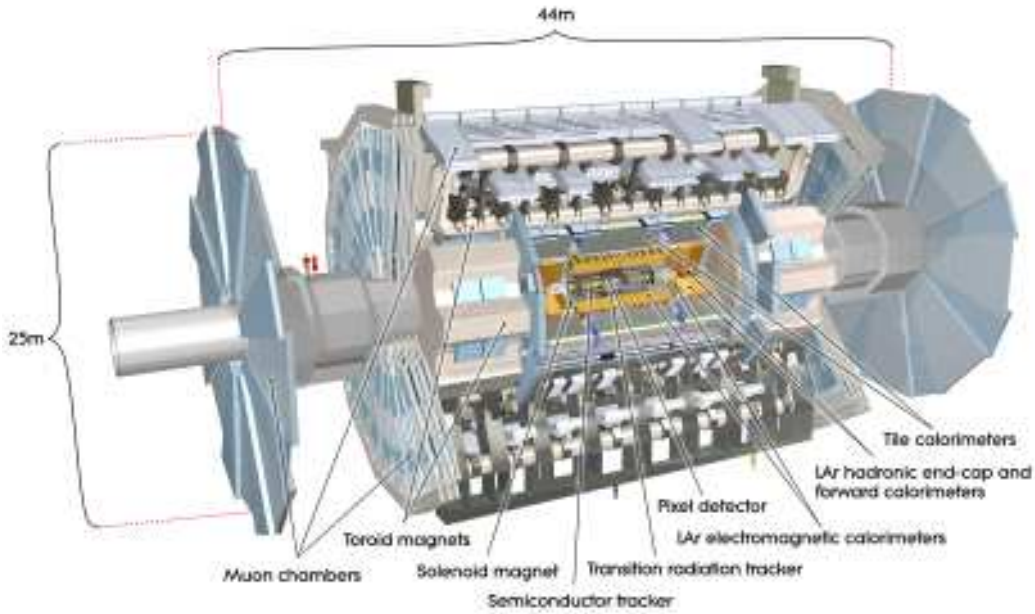


Figure 3.2: View of the ATLAS detector.

The ATLAS detector [49], as shown in Figure 3.2, is a typical 4π detector. Its innermost parts consist of the tracking devices in a 2 T solenoidal magnetic field covering the pseudo-rapidity ($\eta = -\log \tan \theta/2$, θ is the polar angle with respect to the beam axis) of $|\eta| < 2.5$. Electromagnetic and hadronic calorimeters follow further away from the interaction point covering η down to 4.9. The muon detectors are further out in toroidal magnetic field covering $|\eta|$ up to 2.4.

At the LHC the total inelastic cross section for proton-proton interactions is 80 mb. At nominal luminosity every event will be accompanied by an average of 23 minimum bias events. The LHC will collide protons every

25 ns in the center of ATLAS. The high cross section necessitates a fast readout of the detector as well as radiation hard or tolerant electronics for components on the detector.

The tracking detectors are immersed in a solenoidal field of 2 T. It is expected that 1000 particles will come from the collision point with a frequency of 40 MHz within a pseudo-rapidity of 2.5, thus the track density will be large. The innermost tracking device is the Pixel detector, which is segmented in $R-\phi$ and z . Each track crosses three pixel layers, the innermost is at a radius of 5 cm. The intrinsic accuracy in the barrel is $10\ \mu\text{m}$ in $R-\phi$ and $115\ \mu\text{m}$ in z from 80.4 million readout channels.

The Pixel detector is followed by the SCT, consisting of silicon strips with a slightly coarser granularity. The intrinsic accuracy in the barrel is $17\ \mu\text{m}$ in $R-\phi$ and $580\ \mu\text{m}$ in z . There are 6.3 million readout channels for the SCT.

The TRT provides more points for tracking than the Pixel and SCT, however each point has less precision. On average 36 points are provided for tracking with $R-\phi$ information with an intrinsic accuracy of $130\ \mu\text{m}$ per straw up to $|\eta| < 2$. Yet no information is available in the z direction. The TRT has 351000 channels. In addition to its tracking capabilities the TRT also provides particle identification. The TRT measures the transition radiation which is expected to yield a higher signal for electrons than for pions. This information is used for the identification of electrons described later in this Chapter.

The resolution for the tracking detectors has been determined in a realistic simulation of the ATLAS detector. Using the parametrization $\sigma_X = \sigma_X(\text{inf})(1 \oplus p_X/p_T)$, where $\sigma_X(\text{inf})$ is the asymptotic resolution at infinite momentum and p_X is a constant for which the intrinsic and multiple-scattering terms are equal. The resolution in the barrel in simulation correspond to $\sigma_X(\text{inf}) = 0.34\ \text{TeV}^{-1}$ and $p_X = 44\ \text{GeV}$. For a transverse momentum of $100\ \text{GeV}/c$, the relative transverse momentum resolution $p_T \cdot \sigma(1/p_T)$ is about 0.04.

The electromagnetic calorimeter of ATLAS is a sampling calorimeter. The passive material is lead (and stainless steel for the mechanical stability). The active material is Liquid Argon, operating at a temperature of about 90 K. The particularity of the design is the accordion structure as shown in Figure 3.3 ensuring a coverage in ϕ without dead zones. The depth of the calorimeter varies roughly, as function of η , from $25\ X_0$ to $30\ X_0$. An electrical field of 2 kV is applied in the 2 mm Liquid Argon gap.

The calorimeter has three segments in depth providing η coverage up to

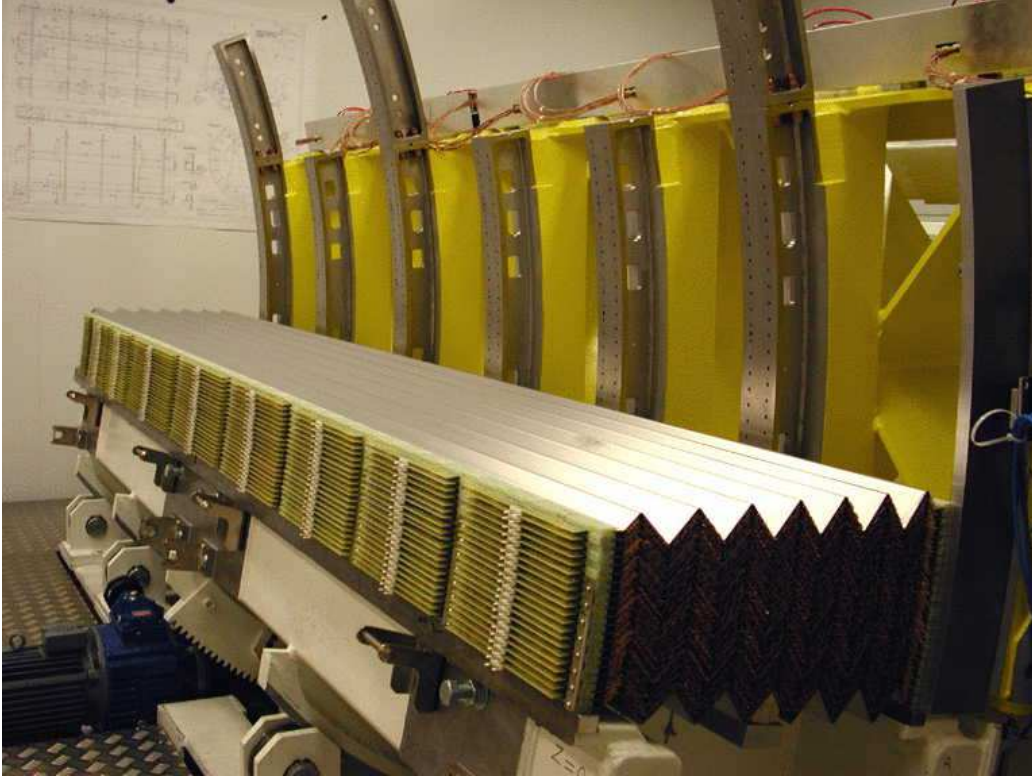


Figure 3.3: View of a module of the accordion calorimeter of the ATLAS barrel during assembly.

3.2 in addition to a presampler (PS) covering $|\eta| < 1.7$. The first segment, the strips, typically has a cell size of $\Delta\eta = 0.003$, coarser in ϕ with a size of 0.1. The fine granularity allows to separate efficiently photons from π^0 . The main part of an electromagnetic shower is deposited in middle section where the typical readout cell size in η and ϕ direction is 0.025×0.025 . The thin back section has the same cell size in ϕ as the middle and is coarser in η with a cell size of 0.05. The expected energy resolution for electrons and photons is $10\%/\sqrt{E}$ and a global constant term of 0.7 % must be achieved. The linearity is required to be of the order of a per mil or better to measure precisely the absolute masses of particles.

The hadronic and forward calorimeters in the endcap are also based on Liquid Argon technology. The absorber of the hadronic calorimeter is made of copper. The calorimeter has four segments in depth. Their size in $\Delta\eta \times \Delta\phi$

is 0.1×0.1 in the region of $|\eta| < 2.5$ and 0.1×0.2 at larger η for a total of 5632 readout channels. The forward calorimeter (FCAL) consists of three high-density modules. The first one, for electromagnetic measurements, is made of copper, the other two are made of tungsten. Concentric rods and tubes are installed parallel to the beam axis. The gap between rod and tube, filled with Liquid Argon as the sensitive material can be as small as 0.25 mm. This ensures a fast signal in the forward region where the pileup effects are expected to be stronger.

The tile calorimeter is situated behind the electromagnetic calorimeter in the barrel. Scintillating tiles provide the signal of the sampling calorimeter while steel is used as absorber. Three layers are provided in depth. The readout cells are of size 0.1×0.1 in the first two layers and 0.1×0.2 in the last layer. Measured in interaction lengths, the tile calorimeter is almost 10λ deep at $\eta = 0$.

The muon system provides coverage for $|\eta| < 2.7$. The muons are deflected in large air core toroids. 1800 hall sensor monitor the magnetic field. Monitored drift tubes are used over most of the η range to provide information for the track reconstruction, cathode strip chambers are used in the endcap due to the higher occupancy. Resistive plate chambers (barrel) and thin gap chambers (endcap) are used for triggering.

ATLAS uses a three stage trigger system to reduce the rate from 40 MHz in level-1 to 75 kHz and further down to 200 Hz in the two high level trigger systems using the full detector information.

3.2.1 Electromagnetic Test beam

A vigorous test beam program has been pursued by ATLAS. Components of all sub-detectors have been tested. A pre-series module of the electromagnetic calorimeter was tested in the test beam with electron beams of fixed energy from 10 GeV to 245 GeV. Four barrel modules, corresponding to 12.5% of the barrel calorimeter and three endcap modules (19% of the endcap calorimeters) which are now installed in ATLAS have also been tested.

The main results of this test beam campaign of nearly five years (1998–2002) have been reported in Refs. [50, 51, 52, 53, 54, 55, 56]. The uniformity, i.e., the variation of the calorimeter response for a fixed energy of 245 GeV, in a barrel module of effective size $\Delta\eta \times \Delta\phi = 1.2 \times 0.2$ is better than 0.5%. The uniformity of the calorimeter is especially important for the measure-

ment of thin resonances, e.g., the Higgs boson decaying to two photons, or sharp endpoints (the lepton–lepton invariant mass in a supersymmetric decay chain). If the intrinsic width is smaller or about equal to the uniformity, the width of the distribution, e.g., of the invariant photon–photon mass, will be dominated by the detector effects. The result obtained is in excellent agreement with the requirements set forth before the construction of ATLAS started: uniformity in a region of 0.2×0.4 better than 0.5%. The number shows the excellent control of the long and difficult production process of all components of the electromagnetic calorimeter.

In addition to the uniformity the energy resolution with its sampling term and local constant term contributes to the width of the measured invariant masses and edges. In the test beam the energy resolution was measured to be (at a fixed η position) better than $10\%/\sqrt{E}$ and the local constant term to be better than 0.3%. The performance expected for the electromagnetic calorimeter of ATLAS has been achieved.

While uniformity and energy resolution determine the width, the energy scale (or central value) needs to be known precisely. Therefore the linearity of the calorimeter is very important. The linearity was measured to be of the order of 2 per mil in a range from 20 GeV to 180 GeV in a special test beam setup.

The test beam has been tremendously important to develop the methods for reconstruction of electrons and photons. However the results obtained with the modules now installed in the ATLAS detector cannot be transferred directly from the test beam to ATLAS, because the material distribution in the test beam is quite different from the one in situ in ATLAS. The strategy chosen was to develop the methods on the test beam, optimize the test beam Monte Carlo, heavily used for the linearity study, and apply the methods to the simulation of the full ATLAS detector. The Monte Carlo provides the (indirect) link between the test beam and the (future) ATLAS data.

In order to have a reliable measurement from the electromagnetic calorimeter it is also necessary to monitor every aspect (stability of the electronics system etc). The dependence of the energy response as function of the liquid Argon temperature has been measured to be 2%/K for a fixed beam energy of 245 GeV. The temperature stability in the test beam cryostat was shown to be better than 7 mK. The Front End electronics, in particular the Front End boards (FEBs) where the signal is amplified, formed and digitized, were tested and their design was validated.

3.2.2 The Front End Board of the LAr Calorimeters

The Front End Electronics of ATLAS consist of several components. Here, as an example the Front End Board (FEB), described in detail in Ref. [33] is discussed. The FEB is located at large radius on the cryostat in the transition region between barrel and endcap. It amplifies the signal of the Liquid Argon detectors of ATLAS, with the exception of the HEC, where the amplifiers are located inside the cryostat.

After preamplification the FEB forms the triangular ionization signal into a bipolar shaper where the peak of the signal is reached typically after 50 ns. This corresponds to only 2 bunch crossings, whereas the ionization signal has a duration of approximately 450 ns. Additionally the bipolar shaping allows to treat the minimum bias/pileup events, which are typically at low transverse momentum, as an additional noise contribution to the resolution of the electromagnetic calorimeter. The shaper also serves as a first step summing device for the trigger. The analog signal is then sampled at 40 MHz and saved in a switch capacitor array (SCA) for about $1.5 \mu\text{s}$ until the first level trigger decision is received. Upon a trigger, the signal is digitized and sent to the Read Out Device (ROD) via an optical link.

The FEB treats 128 readout channels of the calorimeter. 1627 FEBs were produced and configured in 19 different flavors. The production, assembly and test was shared among three labs: NEVIS (University of Columbia), Brookhaven National Laboratory (BNL) and LAL. While NEVIS was responsible for the production and the first digital tests, LAL and BNL each configured, tested and assembled 50% of the FEBs. The operation lasted for almost a year. Three engineers, three technicians and a physicist were involved in the development, maintenance, improvement and functioning of the test setup up at LAL alone. This allocation does not cover the 10 years of R&D of the FEB components in radiation tolerant technology (see [33] for more details).

At LAL, the FEBs were tested one by one in specially developed test stand. The shaper output is in three gains. First the pedestals and the electronic noise were measured. The distribution of the noise RMS of the high gain channel is shown in Figure 3.4 for all FEBs of a flavor. This test allowed to detect dead channels.

To test the signal integrity, a calibration pulse was sent through the electronics chain and the signal was recorded in steps of 1 ns with interleaved events as shown in in Figure 3.5. The analysis of the signal form yielded in

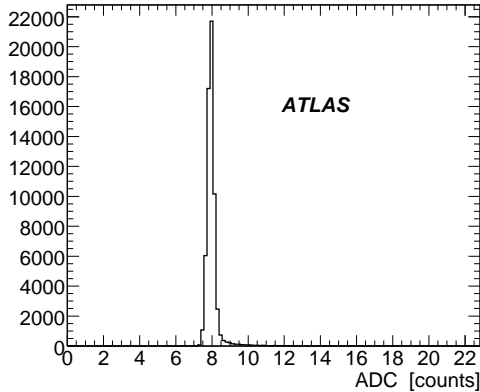


Figure 3.4: Distribution of the noise RMS in ADC counts of the High Gain for a flavor of the FEB (from [33]).

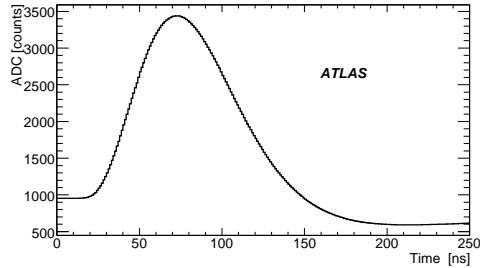


Figure 3.5: Reconstructed signal of the FEB in medium gain as function of the time (from [33]).

particular the time of the signal peak. The peak was required to fall into an acceptance window 7 ns long. The minimum and maximum of the time window were fixed to be the same for all FEBs of the same preamplifier flavor. A wrong time constant of the shaper, usually observed as a signal reaching its maximal amplitude before the minimum time required, was detected this way.

The distribution of the measured linear part of the gain is shown in Figure 3.6. The slope is sensitive for the detection of dead channels, accelerated shaper timing and channels with linearity problems. In normal running in ATLAS only one of the three gains is read out. The gain choice is made by a dedicated chip (GSEL) on the FEB. The integrity of the choice, corresponding in practice to the setting of two thresholds in the medium, was verified.

The FEB provides the signals for the trigger level-1. In order to avoid excessive triggering due to noisy channels, individual calorimeter readout cells can be turned off. Figure 3.7 shows the test for one FEB as example. This test also checks the correct signal routing of the trigger signals on the FEB. Additionally the gains as well as the shapes of the trigger outputs were measured and compared to references as well.

On the 786 boards configured and tested at LAL with roughly 75000 shapers, SCAs and Preamplifiers, 801 repairs had to be performed. Part of

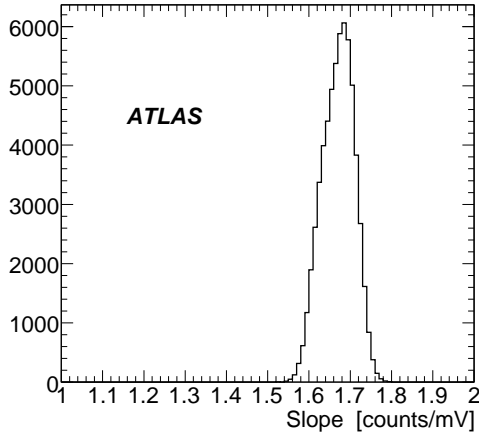


Figure 3.6: Distribution of the Low Gain slope from a linear fit for a FEB flavor (from [33]).

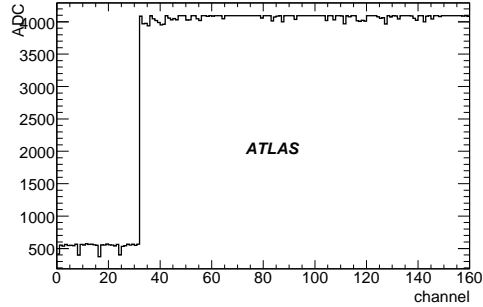


Figure 3.7: Test of the FEB trigger output. No signal is expected for the first 32 entries and for the next 128 entries a large signal should be observed (from [33]).

the repairs (faulty chip replacement) was performed in industry, another part in house.

The FEBs are cooled with water circulating in plates which are mounted individually on each FEB. To test that the system has no leaks, an air pressure test at 3 bar was performed. The water system in the experiment is an under-pressure system which ensures that, in case of a leak, air would enter the system, but no water would flow out. The FEBs were shipped to CERN after a further functional verification.

Since the completion of this operations the test bench has been kept functional. It was used again in 2008/2009 for a small production of about 40 additional boards. After more than a year of operation on the detector several boards were malfunctioning due to corrosion. The corrosion was traced to an error in the cleaning procedure after chip replacement at the subcontractor. In addition the peaking time of the signal was unstable over time. The FEBs were removed from the detector, cleaned if necessary, or replaced. The peaking time of the shaper was stabilized by cutting pin connections between the shaper and FEB board (1627 boards times 32 circuits

per board).

The production, assembly and test of the FEBs was a difficult endeavor. It was a successful operation as the time delay given by the collaboration was respected. A large number of problems on the boards were detected and repaired before installation.

3.3 Performance of the ATLAS Detector

The first physics results expected from collision data will be essential to prepare the physics calibration and measure the performance in situ. In order to evaluate the current understanding of these issues, physics studies and a test of the analysis model, ATLAS has performed a Computing System Commissioning (CSC) evaluation [31].

For the CSC studies more than 25 million events were simulated, digitized and reconstructed. The event samples comprised single particles, essentially for calibration and identification, as well as complex physics events at the nominal center-of-mass energy of 14 TeV. The best known description of the detector, including the experience gained from the test beam studies of all sub-detectors, was used in the simulation.

Muons are reconstructed with an efficiency of more than 95% for tracks with transverse momenta of more than 5 GeV/ c . Good coverage in η is obtained in combination with a low fake rate as shown in Figure 3.8 (Left). Muons can be reconstructed in the muon spectrometer alone as well as in the inner detector. The combination of the two significantly reduces the fake rate by an order of magnitude. In order not to rely on Monte Carlo for the determination of the efficiency, the production and decay of the Z boson will be used. With an integrated efficiency of 100 pb⁻¹, using the well known Z boson mass, a statistical precision of 0.1% and a systematic error of 1% can be obtained. With only half as much integrated luminosity the muon energy scale will be known with an accuracy of ± 0.5 GeV for transverse momenta of 50 GeV/ c .

Jet reconstruction is performed in several stages. First clusters are reconstructed in the calorimeters and calibrated locally [31]. Jets are then reconstructed with a jet algorithm, most frequently the cone and the kt algorithms though others are also under study. Noise, pileup and the underlying event are corrected for as the last step. The jet energy scale, as shown in Figure 3.9, is correct at the percent level. Photon plus jet events and Z boson

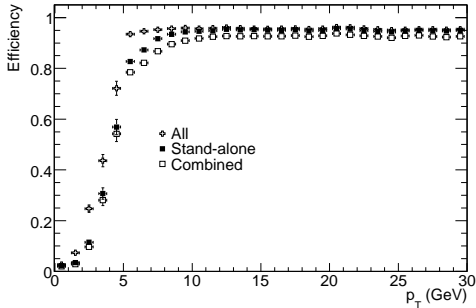


Figure 3.8: (The efficiency for reconstructing muons is shown as function of the transverse momentum for the muon spectrometer reconstruction, combined reconstruction and combined with the use of segment tags (taken from [49]).

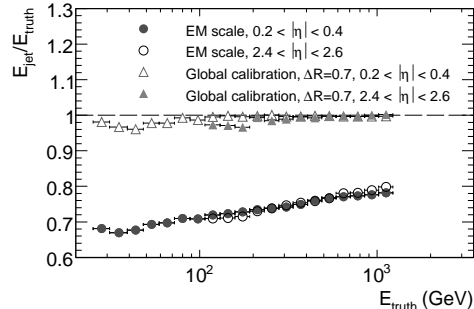


Figure 3.9: The signal linearity of jets reconstructed with $R_{\text{cone}} = 0.7$, in two different regions of $|\eta|$ is shown as a function of E_{truth} for jets at the electromagnetic energy scale and fully calibrated jets (taken from [49]).

plus jets will be used to carry out the in situ calibration. Due to the large production cross sections, only 10 pb^{-1} will be necessary to reach a percent precision for low (less than 80 GeV) transverse energies.

In the E_T^{miss} reconstruction the energy deposits in the readout cells of the calorimeters are refined by the identification of muons, electrons and jets. Not using this knowledge would lead to an offset of about 30% with respect to the true missing energy. The linearity is about 5% and the E_T^{miss} resolution is expected to be $0.57 \cdot \sqrt{\Sigma E_T}$, as shown in Figure 3.10. The scale will be verified for low E_T^{miss} with the Z boson decaying to taus.

The hadronically decaying taus are either reconstructed by a tracking based or a calorimeter based algorithm with an efficiency of 30% for a jet rejection of 10^3 . Clean samples of taus will come from the production of the W and Z bosons. The visible mass reconstructed from a leptonically and a hadronically decaying tau will peak at about $54 \text{ GeV}/c^2$. This can then be used for the calibration of the hadronic τ decay.

For b-tagging a working point at 60% efficiency is defined, where the rejection of light jets is about 30 for the simplest algorithm. Using the longitudinal and transverse impact parameter significance, the rejection is increased by a factor two. Reconstruction of the secondary vertex leads to

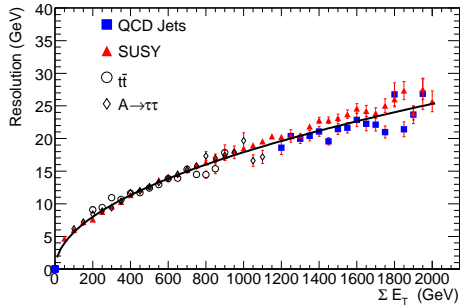


Figure 3.10: The resolution of the E_T^{miss} vector is shown for QCD di-jet events and Higgs bosons (A) including a parametrization $0.57\sqrt{\Sigma E_T}$. (taken from [49]).

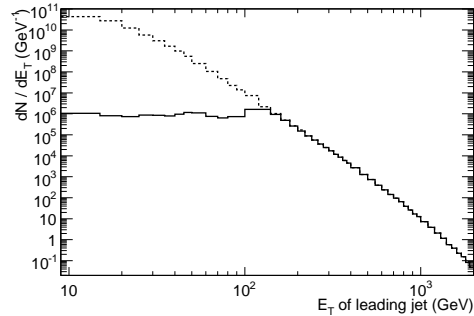


Figure 3.11: The expected differential spectrum for single jets is shown after the level-1 trigger and pre-scale factors as well as without (taken from [49]).

a light jet rejection of 150. The b-tagging performance will be calibrated in situ with top quark pair production to a precision of 5–10% and with muon plus jets at low momentum.

Trigger menus have been developed for different values of the instantaneous luminosity, expected to be several orders of magnitude below the nominal $10^{34} \text{cm}^{-2} \text{s}^{-1}$ at startup. The total rates are within budget and the turn-on curves are reasonably sharp. Differential jet production will be measured over many orders of magnitude, as shown in Figure 3.11.

3.3.1 Electron and Photon Reconstruction

The reconstruction, calibration and identification of electrons and photons are an example of the transfer of test beam knowledge to ATLAS simulation and reconstruction.

In the standard algorithm for isolated electrons and photons, clusters are reconstructed from calibrated readout cells. The cluster algorithm uses a fixed size, independent of the energy of the cluster. A track is then matched to the cluster geometrically and uses the ratio of calorimetric energy to tracker momentum. To qualify the candidate as electron candidate the track is required not to be associated to the reconstructed conversions. Conversions are reconstructed independently in the tracking system alone. Clusters with conversion tracks and/or clusters without associated tracks are classified as

photon candidates.

For the calibration the difficulty lies in the simultaneous optimization of resolution and linearity (energy scale). Two methods of electron and photon calibration have been developed to address this problem. The first one is a weighting technique which uses the presampler and the energy deposited in the calorimeter segments to derive from Monte Carlo the correction factors to be applied. These factors correct for the energy loss upstream of the calorimeter. The material in front of the calorimeter (inner detector, services, mechanical structures) is several radiation lengths, leading to bremsstrahlung and photon conversions. The second method uses the Monte Carlo to correlate the energy lost with the shower depth and derive a correction (dead matter calibration). The application of these methods leads to a linearity of the order of per mil up to several hundred GeV. In addition to this longitudinal weighting, local corrections are also applied to correct the cluster position as well as to correct for the local energy variations. For details see Ref. [31].

As the cross-sections for QCD jet production are several orders of magnitude larger than, for example, the production of the Z boson decaying to electrons, a high jet rejection is necessary while maintaining high efficiency. The electron and photon identification is based on the use of the shower shapes, calculated from the order 100 readout cells building an electromagnetic cluster, from tracking information and from track-matching information. In particular on the tracking side the TRT transition radiation measurement is used to differentiate between charged pions and electrons. On the calorimeter side the fine granularity of the first calorimeter segment (strips) allows to reduce the pion (decaying to two photons) by a factor three.

The differential jet cross sections drop sharply as function of the transverse energy. The cross section for some discovery channels of new physics might be large. On the other hand, sensitivity to rare new physics processes with electrons and photons must be retained. These different needs led ATLAS to define three electron identification qualities, one (tight) with the highest possible jet rejection of 10^5 , a second one (medium) with a rejection of 2200 (with higher efficiency) and third one with a jet rejection of 570. The corresponding efficiencies are shown in Figure 3.12 as function of the transverse energy. For photons a jet rejection of 8000 has been obtained for an efficiency of 85%.

The Z boson data will be essential to determine the electron reconstruction and identification efficiency in situ. One electron is well identified (tag)

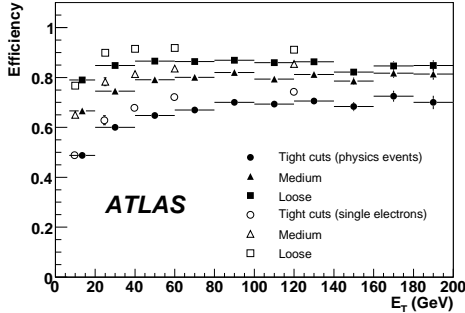


Figure 3.12: The electron efficiency is shown as function of the transverse energy (taken from [31]) for supersymmetric events as well as single particles.

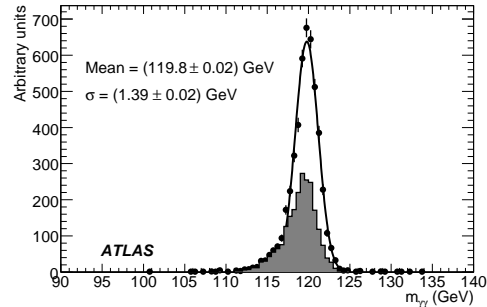


Figure 3.13: The reconstructed Higgs mass is shown. The shaded histogram are the events where at least one photon has converted (taken from [31]).

and the other electron is used to study the efficiency (probe). Good agreement is obtained between the tag&probe method and Monte Carlo truth. A statistical error on the efficiency of $\pm 0.1\%$ and a systematic error of $\pm 1.5\%$ can be obtained with an integrated luminosity of 100 pb^{-1} .

The Monte Carlo can only help to determine the best possible reconstruction for the linearity. The absolute scale must be determined by using the process $Z \rightarrow ee$. The ATLAS electromagnetic calorimeter has a uniformity of 0.5% in regions of $\Delta\eta \times \Delta\phi = 0.2 \times 0.4$, as shown in the test beam studies. These regions are inter-calibrated to obtain a long range constant term of about 0.4% with an integrated luminosity of 100 pb^{-1} . Thus the goal of a global constant term of 0.7% is within reach.

As an illustration of the performance of the electron and photon reconstruction the reconstructed invariant mass of the photons from the decay of the Higgs boson to two photons is shown in Figure 3.13. The energy scale is correct to about 500 MeV . The shaded area are events where at least one of the photons has converted.

In addition to the standard algorithm described here, a second algorithm, more appropriate for the reconstruction of non isolated electrons, e.g., in the vicinity of jets, has also been developed by ATLAS. As the first source of electrons at the LHC will be the copious production of electrons from $J/\psi/\Upsilon$ decays with rather low transverse energy, it will be useful to use the two

algorithms to study the overlap and possible improvements.

The lessons learned from test beam measurements have been transferred successfully to the reconstruction of physics events simulation with a detailed description of the ATLAS detector. The performance of the reconstruction, e.g., electrons and photons, is in agreement with expectations providing a good basis for future studies and most importantly the collision data from 2009 on.

3.4 e^+e^- Linear Collider

Two designs for a linear collider are being pursued currently: ILC and CLIC. The ILC is an e^+e^- collider design with a center-of-mass energy of 500 GeV upgradable to 1 TeV [57]. While the nominal center-of-mass energy is lower than that of the LHC, all the energy is available in the collisions in contrast to the LHC. The properties of an e^+e^- collider complement the LHC studies. Therefore the ILC is considered to be the next project for high energy physics, depending on the results obtained by the LHC.

The layout of the ILC is shown in Figure 3.14. The tunnel length is about 31 km. Electrons and positrons are accelerated in tunnels of 11 km length. The beam delivery system is about 4.5 km long. The crossing angle is planned to be 14 mrad. Two detectors will be installed in a push-pull system, alternating their data-taking periods.

The main technological challenge of the ILC is the acceleration of the electrons, whereas at the LHC the challenge is the magnet system. The ILC design calls for the use of superconducting cavities, operating at a frequency of 1.3 GHz, with an average gradient of 31.5 MeV/m. In addition to this challenge, it is planned to have an electron polarization of more than 80%. The positrons are produced by conversion of photons (passing the electron beam through an undulator) into e^+e^- pairs. The current design of the machine has a positron polarization of 30%, which in a upgrade could be increased to 60%. The polarisation must be measured with a precision of 0.1% via the compton effect.

The center-of-mass energy can be varied from 200 GeV to 500 GeV. Short periods at 91 GeV (Z-resonance) for calibration will also be possible. The precision of the knowledge of the beam energy will feed directly into the absolute uncertainty of the measurement of any particle mass. It is expected to be able to measure the beam energy to 200 ppm by using two different

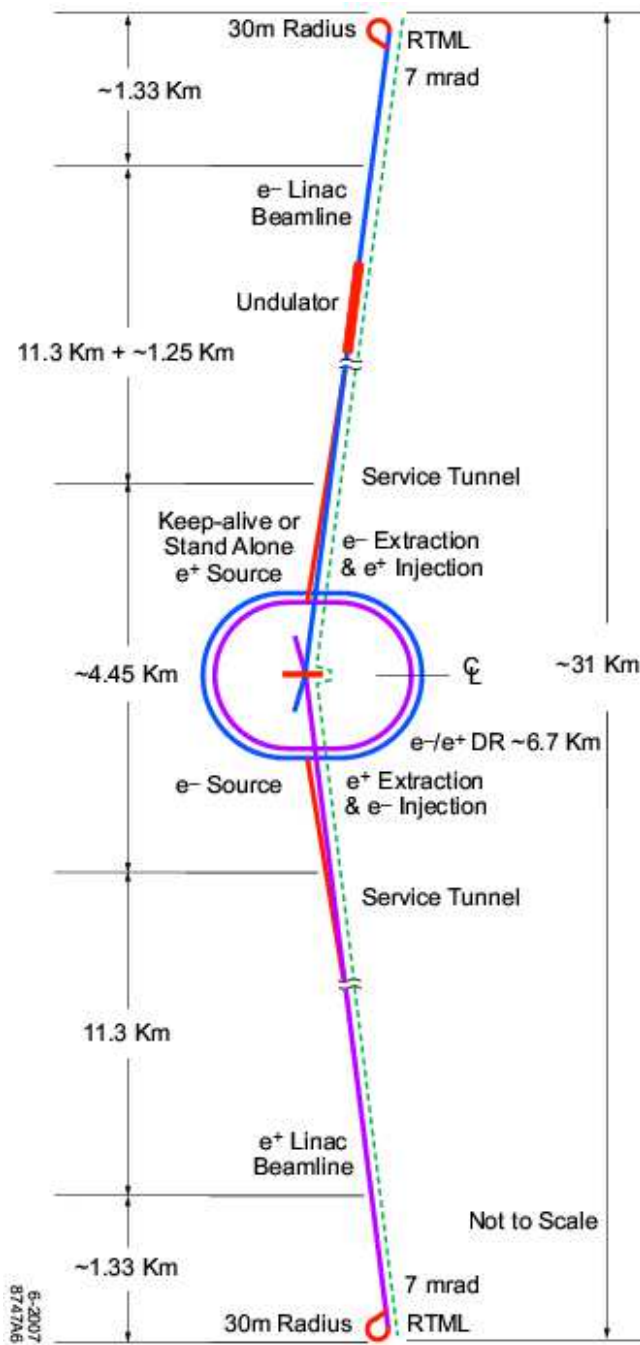


Figure 3.14: Layout of the ILC.

methods. Upstream the deflection of the beam through a dipole field will be measured. Downstream the synchrotron radiation of the beam passing through a string of dipole magnets will be measured. The beam has a pulse rate of 5 Hz with a pulse length of about 1 ms. In each pulse there will be 2625 bunches with $2 \cdot 10^{10}$ particles per bunch. The design luminosity of the ILC is $10^{34} \text{m}^{-2} \text{s}^{-1}$. The RMS of the beam size at the interaction point is expected to be about 6 nm (vertical) and about 640 nm (horizontal). In addition to initial state radiation, 2.4% (RMS) of the energy will be lost due to beamstrahlung. The downstream beam energy measurement will measure the beam energy spread as well as the beam energy distribution after beamstrahlung has occurred.

While the preparation of the ILC is well advanced, R&D is also performed for a collider further in the future. A second generation e^+e^- collider called CLIC ([60] and references therein) is being developed. The CLIC concept is based on a novel scheme decelerating one beam to accelerate another one. CLIC has the potential to reach a center-of-mass energy of 3 TeV.

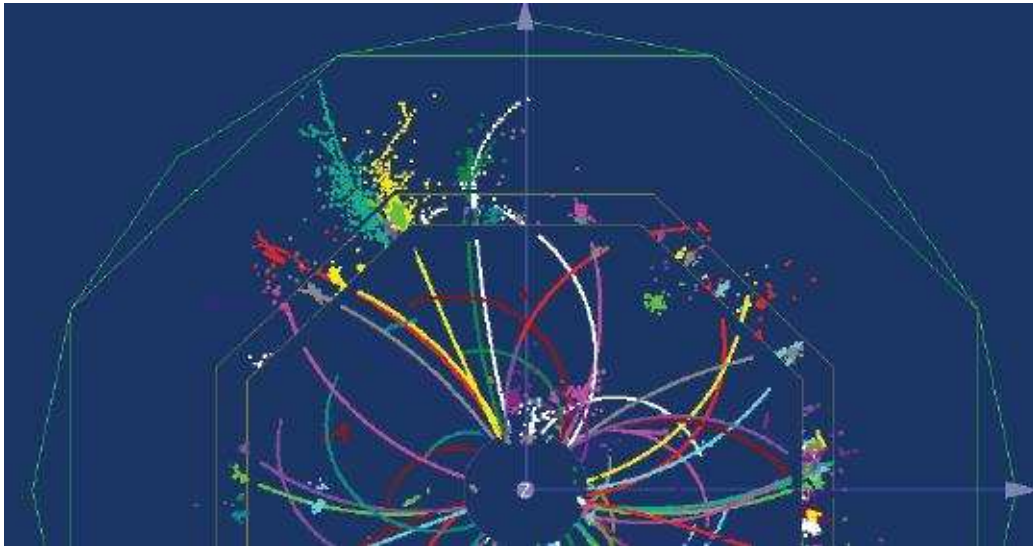


Figure 3.15: Event display of a simulated event in a detector for the ILC. The fine granularity of the calorimeter used in the particle flow is clearly seen.

Currently there are three detector concepts under study, competing for

the two ILC detector spots. The two main ones are ILD (International Linear Detector) [58] and SiD (Silicon Detector) [59]. They differ in the technology chosen for the tracking sub-detectors. SiD has silicon based tracking with a strong magnetic field of 5 T, thus choosing to build a compact detector. ILD has chosen a larger volume design with a lower magnetic field of 4 T and with a large gaseous TPC in addition to the silicon vertex detector. The goal for the tracking system is to reach a precision of $\sigma(1/p_T) = 10^{-4}\text{GeV}^{-1}$ above 10 GeV/c, an order of magnitude more precise than the precision achieved by the LEP detectors.

The calorimeters chosen by both collaborations are similar: the electromagnetic calorimeter is a very high granularity detector. For this reason it is sometimes called tracker-calorimeter, with 100 million readout channels (the ATLAS electromagnetic calorimeter has about 150000 readout channels). The energy resolution for electrons is about $15\%/\sqrt{E}$ for electrons, which is less ambitious than LHC experiments (e.g. ATLAS 10% or CMS 2%). However the main physics processes expected at the ILC are multi-jet processes where the individual performance is less important than the combined reconstruction of all sub-detectors in the particle flow concept. A jet resolution using Particle Flow of $30\%/\sqrt{E}$ is expected, improving on the 50% expected in ATLAS. An event display showing the fine granularity of the electromagnetic calorimeter is shown in Figure 3.15.

Chapter 4

Determination of Supersymmetric Parameters and Higgs Couplings

The determination of the fundamental parameters, be it supersymmetric parameters or the Higgs couplings, critically depends on detailed experimental simulations of measurements and errors at the LHC and at the ILC. While the techniques described here are general, the well-understood parameter point SPS1a [45] is used as a specific example. This point has a favorable phenomenology for both LHC and ILC.

SPS1a was invented as a parameter set for the study of the LHC and ILC discovery and measurement potential. The Standard Model electroweak measurements, the b-physics precision observables, $(g - 2)_\mu$ [78] with the addition of the WMAP [77] measurement of the relic density already allows to delimit interesting regions of parameter space without the direct observation of supersymmetric particles. In particular, as shown in [79, 80], the supersymmetric mSUGRA fit of these observables results in a preferred value for the lightest Higgs boson mass of $m_h = 113.3 \text{ GeV}/c^2$, pushing the Higgs boson mass closer to the limit of direct searches at LEP of $114.4 \text{ GeV}/c^2$ [18]. The effect of using the LEP exclusion is about $3 \text{ GeV}/c^2$. The best-fit point is close, albeit with rather large errors, to the definition of SPS1a [81]. This is a further motivation to study the phenomenology of this parameter set in detail. Using a different technique, the MSSM parameters have been studied using the precision observable as shown in Ref. [82].

Discovering supersymmetry, and in particular SPS1a, at the LHC is con-

sidered to be feasible for masses up to $2.5 \text{ TeV}/c^2$ (squarks and gluinos). In general, supersymmetry provides signatures with several high-pT jets and large missing energy. The search for the lightest Higgs boson around the LEP limit is considered to be more difficult. It necessitates more statistics (around 30 fb^{-1}) than for supersymmetry, where 1 fb^{-1} are sufficient to be sensitive to masses of squarks of several hundred GeV/c^2 . The complexity in the Higgs sector is due to the necessity to search for rare, but clean final states ($\gamma\gamma$) in large QCD/Standard Model backgrounds. Once the new particles are discovered, detailed measurements can be performed.

To reconstruct the fundamental parameters, precise theoretical predictions are necessary. An overview of the tools is given in Ref. [61]. The production rates for the Higgs boson are taken from [89]. The most important in the supersymmetric sector are SuSpect, SOFTSUSY and SPheno [62, 63, 64] for the calculation of the sparticle and Higgs masses. SUSY-Hit provides the branching ratios via SDecay for the decay of supersymmetric particles and HDecay for the decays of the Higgs bosons [65, 66, 67]. e^+e^- cross sections are calculated by PYTHIA and SPheno [68, 64], while proton-proton cross sections, first calculated in [83], are provided by Prospino2.0 at NLO [69, 70, 71, 72].

The pioneering work on extracting the fundamental parameters was performed in [73, 74], followed by Fittino [75] and SFitter [35]. The package Super-Bayes originated in the study of the dark matter aspect of supersymmetry [76]. Several other projects are also underway.

In this chapter, first the signatures of the Standard Model Higgs boson sector and the supersymmetric signals will be discussed. Then the most favorable case will be studied: mSUGRA including all supersymmetric signals, followed by the study of the weak scale model, the MSSM. As a final study the question of the determination of the Higgs couplings as well as the sensitivity of these to new physics will be addressed. For the latter study the question will be: if new physics signals are not observed at the LHC, will the precision of the measurement of the Higgs boson couplings be sufficient to be sensitive to new physics?

4.1 Low Mass Higgs Boson Signatures

The Higgs boson can be produced in gluon fusion [85], weak boson fusion and top pair production. The expected cross sections are shown in Figure 4.1.

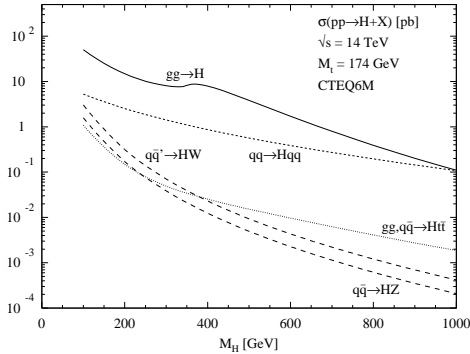


Figure 4.1: The production cross section for a Standard Model Higgs boson at the LHC is shown as function of its mass for the main production mechanisms.

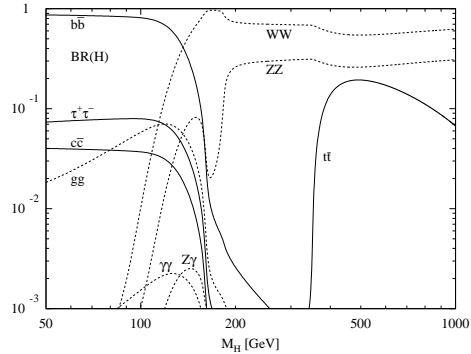


Figure 4.2: The branching ratios of the Standard Model Higgs boson are shown as function of its mass.

While tremendous progress on the understanding of the Monte Carlo modeling of the background processes has been made, it is essential for most of the analyzes to determine the background from the data, e.g., via side-band background subtraction. This means that at the LHC channels with the capability of the reconstruction of the Higgs mass (with the best possible precision) are favored over counting analyses.

The gluon fusion process at the LHC is known with an uncertainty of 13% [136, 137, 138, 139, 140]. NLO corrections [130, 131] as well as NNLO calculations with an effective ggH coupling [132, 133, 134, 135] lead to a cross section of 37 pb for a 120 GeV/ c^2 Higgs boson. For the weak boson fusion process, the cross section is about 4.5 fb [141, 142, 143, 144]. This production mode relies on a central jet veto between the forward tagging jets [145, 146, 147]. For this signal, NLO rates as well as distributions have been calculated [148, 149, 150, 151, 152] and an error of 7% [148, 149, 150, 151, 152] is used.

The production channels of gluon fusion and weak boson fusion are not independent: Higgs boson production with two jets has contributions from both gluon fusion and weak boson fusion. With appropriate cuts, one channel can be enhanced over the other [158, 159]. The error on this classification is covered by the error estimate.

A cross section of 450 pb is expected for the channel ttH , the radiation

production	decay	$S + B$	B	S	$\Delta S^{(\text{exp})}$	$\Delta S^{(\text{theo})}$
$gg \rightarrow H$	ZZ	13.4	6.6 ($\times 5$)	6.8	3.9	0.8
qqH	ZZ	1.0	0.2 ($\times 5$)	0.8	1.0	0.1
$gg \rightarrow H$	WW	1019.5	882.8 ($\times 1$)	136.7	63.4	18.2
qqH	WW	59.4	37.5 ($\times 1$)	21.9	10.2	1.7
$t\bar{t}H$	$WW(3\ell)$	23.9	21.2 ($\times 1$)	2.7	6.8	0.4
$t\bar{t}H$	$WW(2\ell)$	24.0	19.6 ($\times 1$)	4.4	6.7	0.6
inclusive	$\gamma\gamma$	12205.0	11820.0 ($\times 10$)	385.0	164.9	44.5
qqH	$\gamma\gamma$	38.7	26.7 ($\times 10$)	12.0	6.5	0.9
$t\bar{t}H$	$\gamma\gamma$	2.1	0.4 ($\times 10$)	1.7	1.5	0.2
WH	$\gamma\gamma$	2.4	0.4 ($\times 10$)	2.0	1.6	0.1
ZH	$\gamma\gamma$	1.1	0.7 ($\times 10$)	0.4	1.1	0.1
qqH	$\tau\tau(2\ell)$	26.3	10.2 ($\times 2$)	16.1	5.8	1.2
qqH	$\tau\tau(1\ell)$	29.6	11.6 ($\times 2$)	18.0	6.6	1.3
$t\bar{t}H$	$b\bar{b}$	244.5	219.0 ($\times 1$)	25.5	31.2	3.6
WH/ZH	$b\bar{b}$	228.6	180.0 ($\times 1$)	48.6	20.7	4.0

Table 4.1: Signatures used for the analysis for a Higgs mass of 120 GeV/ c^2 . The Standard Model event numbers for 30 fb $^{-1}$ include cuts [86]. The factor after the background rates describes how many events are used to extrapolate into the signal region. The last two columns give the one-sigma experimental and theory error bars on the signal (taken from [36]).

of a Higgs boson from a top quark. NLO rate calculations have been performed [160, 161, 162]. A theory error of around 13% is associated to this channel.

For the associated production of the Higgs boson and a weak vector boson (Z or W), a cross section of 2.2 pb is expected. For this channel a theory error of 7% is assumed.

The analysis will be constrained to the single production of Higgs bosons. Pair production is essentially sensitive to the self-coupling of the Higgs and extremely difficult at the LHC [163, 164, 165, 166, 167, 168, 169, 170, 171].

For a Higgs boson of mass 120 GeV/ c^2 the highest branching ratio is to a pair of b-quarks. The branching ratio is roughly 90% as shown in Figure 4.2. However, discovering the Higgs boson in this decay channel is particularly difficult, because reconstructing a Higgs boson invariant mass peak from two b-jets above the QCD continuum is hopeless. Therefore the

associated production in combination with a pair of top quarks have been studied. The combinatorial background is more complex than previously estimated, making it difficult to establish this signal at the 5σ level [47, 31] for 30 fb^{-1} . This development is taken into account by reducing the signal by 50% with respect to the analysis in Ref. [86].

luminosity measurement	5 %			
detector efficiency	2 %		$\Delta B^{(\text{syst})}$	correl
lepton reconstruction efficiency	2 %	$H \rightarrow ZZ$	1%	yes
photon reconstruction efficiency	2 %	$H \rightarrow WW$	5%	no
WBF tag-jets / jet-veto efficiency	5 %	$H \rightarrow \gamma\gamma$	0.1%	yes
b -tagging efficiency	3 %	$H \rightarrow \tau\tau$	5%	yes
τ -tagging efficiency (hadronic decay)	3 %	$H \rightarrow b\bar{b}$	10%	no
lepton isolation efficiency ($H \rightarrow 4\ell$)	3 %			

Table 4.2: Experimental systematic errors used in the analysis. Left: systematic errors applying to both signal and background. Reconstruction and tagging efficiencies are defined per particle, e.g., $H \rightarrow \gamma\gamma$ has a 4% error on the photon reconstruction. Right: systematic background errors, either fully correlated or independent between channels. Tables are the same as [86, 36].

The decay of the Higgs boson to two photons has the advantage of a precise mass reconstruction. Thus in spite of the low branching ratio of order of 10^{-3} , the excellent mass resolution of the calorimeters at the LHC allows to separate the signal from the background of QCD and prompt photons. As the natural width of the Higgs boson at $120 \text{ GeV}/c^2$ is smaller than the experimental resolution (about $2 \text{ GeV}/c^2$), the uniformity of the calorimeters is essential for the discovery. For the measurement of the Higgs boson mass, once sufficient statistics are accumulated, a precise knowledge of the photon energy scale in the calorimeter is essential. The preparation of this measurement through test beam studies gives additional confidence in this channel. The channel can be measured separately in the gluon fusion, weak boson fusion and top pair production. The expected precision of the mass measurement is $\mathcal{O}(200 \text{ MeV}/c^2)$.

The associated production of ZH or WH was considered to be hopeless initially (in contrast to the TeVatron where it is the main source for the signal search). In a theoretical study the Higgs boson is required to be strongly boosted with an inherent loss of efficiency due to this requirement.

The idea is then to use the subject structure of the Higgs boson decay to gain additional leverage [87] more than compensating the loss of efficiency. This promising new channel is also included in the analysis. The results of the theoretical analysis have been confirmed recently by an ATLAS study at the level of 10% [88].

The branching ratio for Higgs boson to a pair of Z bosons is smaller at 120 GeV/ c^2 than at much higher masses. It is considered to be the golden channel with the Z bosons decaying to electrons or muons. Some information can still be obtained from this channel, either produced in gluon fusion or in weak boson fusion.

The decay of the Higgs boson to two leptonically (electrons and muons) decaying W^\pm bosons is also used in the analysis. This counting analysis, due to the neutrinos in the W^\pm decay, does not allow the reconstruction of the Higgs boson mass. The background is rejected using the angular correlation of the leptons.

The decay of the Higgs boson to a pair of τ -leptons can be used for the weak boson fusion process. Here the Higgs boson is boosted (in contrast to the gluon fusion process) which allows the use of the collinear approximation to reconstruct the Higgs boson mass.

σ (gluon fusion)	13 %	$\text{BR}(H \rightarrow ZZ)$	1 %
σ (weak boson fusion)	7 %	$\text{BR}(H \rightarrow WW)$	1 %
σ (VH -associated)	7 %	$\text{BR}(H \rightarrow \tau\bar{\tau})$	1 %
σ ($t\bar{t}$ -associated)	13 %	$\text{BR}(H \rightarrow c\bar{c})$	4 %
		$\text{BR}(H \rightarrow b\bar{b})$	4 %
		$\text{BR}(H \rightarrow \gamma\gamma)$	1 %
		$\text{BR}(H \rightarrow Z\gamma)$	1 %
		$\text{BR}(H \rightarrow gg)$	2 %

Table 4.3: Theory errors used in the analysis. The left table shows the errors on the production cross section and the right table shows the errors on the branching ratio (taken from [36]).

The production rates for the Higgs sector were calculated in [89] and the branching ratios are taken from HDecay [67, 66]. All rates and experimental errors are effectively taken from [86] (with the exception of the modified $t\bar{t}b\bar{b}$ channel). The expected results are listed in Table 4.1. Experimental systematic errors are shown in Table 4.2 and the theoretical errors are shown

in Table 4.3

At the ILC the mass of a $120 \text{ GeV}/c^2$ Higgs boson can be measured with a precision of about $50 \text{ MeV}/c^2$. The expected precision on the Higgs coupling measurements is at the percent level. Additionally precision measurements of the couplings of the Higgs boson are not restricted to judiciously chosen channels. A model independent analysis of the Higgs production and decay is possible. This can have consequences on the interpretation of the determination of the couplings as will be shown later.

4.2 Supersymmetric Observables for a specific Parameter Set

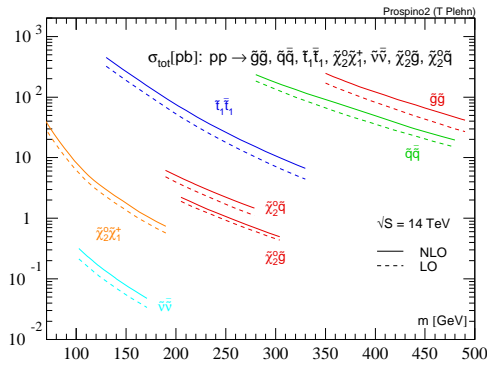


Figure 4.3: The production cross section for supersymmetric particles at the LHC at NLO is shown as calculated by Prospino2.0.

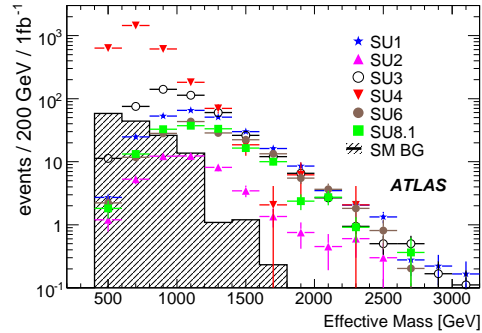


Figure 4.4: The effective mass is shown for the Standard Model and several supersymmetric parameter sets in ATLAS.

The parameter point SPS1a is characterized by moderately heavy squarks and gluinos, which leads to long cascades including neutralinos and sleptons. The mass of the lightest Higgs boson is close to the mass limit determined at LEP.

The production of squarks and gluinos and their decay lead to large signals (in contrast to the Higgs sector) above the Standard Model background. The NLO cross sections calculated by Prospino2.0 are shown in Figure 4.3. The production cross sections for strongly interacting particles are several

tens of picobarn. Inclusive analyses such as the search for highly spherical events with large missing transverse energy (due to the LSPs) and several jets with high transverse momenta, and/or adding the requirement of a lepton (or more) will allow the discovery of supersymmetry. The effective mass, the sum of the jet transverse momenta and the missing transverse energy, will give a first hint of the scale of supersymmetry. An example for the effective mass of supersymmetric signals and Standard Model background is shown in Figure 4.4. At large effective mass the supersymmetric signal dominates the distribution. It is essential to have a good understanding of the jet and ET_{miss} reconstruction to have confidence in the discovery. In the standard scenarios the LHC will be sensitive to squark and gluino masses up to $2.5 \text{ TeV}/c^2$.

An important aspect of subsequent measurements of the supersymmetric particles is the long decay chain [106, 107]

$$\tilde{q}_L \rightarrow \chi_2^0 q \rightarrow \tilde{\ell}_R \ell q \rightarrow \ell \ell q \chi_1^0. \quad (4.1)$$

The final state contains at least a hard jet and two opposite sign same flavor leptons. In this decay chain five edges and thresholds can be calculated and reconstructed [46]. One of the invariant mass combinations is the lepton–lepton edge. As shown in Table 4.4, with an integrated luminosity of 300 fb^{-1} , the measurement is not statistics limited, but limited by the knowledge of the lepton energy scale. Thus attaining the goal of a per mil level energy scale is important and justifies the tremendous work performed on this issue in test beam and Monte Carlo simulations.

The edges and thresholds can be expressed as functions of the four intervening masses. Therefore from the system shown in Table 4.4 the masses of the supersymmetric particles can be reconstructed, using either via toy Monte Carlo or a fit. It is important to note that there is no assumption is made on the underlying theory. Further signatures, e.g. the squark-R and the sbottoms, provide a total of 14 observable and measurable particles at the LHC in SPS1a. The precision of the mass determination for the LHC is shown in Table 4.5. Typically the systematic error on measurements at the LHC coming from the jet energy scale is 1% and 0.1% for the lepton energy scale. These energy–scale errors are each taken to be 99% correlated separately as discussed in Ref [46]. With integrated luminosities of up to 300 fb^{-1} the statistical error in many cases is smaller than the systematic error.

type of measurement		nominal value	stat.	LES	JES	theo.
			error			
m_h		108.99	0.01	0.25		2.0
m_t		171.40	0.01		1.0	
$m_{\tilde{l}_L} - m_{\chi_1^0}$		102.45	2.3	0.1		2.2
$m_{\tilde{g}} - m_{\chi_1^0}$		511.57	2.3		6.0	18.3
$m_{\tilde{q}_R} - m_{\chi_1^0}$		446.62	10.0		4.3	16.3
$m_{\tilde{g}} - m_{\tilde{b}_1}$		88.94	1.5		1.0	24.0
$m_{\tilde{g}} - m_{\tilde{b}_2}$		62.96	2.5		0.7	24.5
m_{ll}^{\max} :	three-particle edge($\chi_2^0, \tilde{l}_R, \chi_1^0$)	80.94	0.042	0.08		2.4
m_{llq}^{\max} :	three-particle edge($\tilde{q}_L, \chi_2^0, \chi_1^0$)	449.32	1.4		4.3	15.2
m_{lq}^{low} :	three-particle edge($\tilde{q}_L, \chi_2^0, \tilde{l}_R$)	326.72	1.3		3.0	13.2
$m_{ll}^{\max}(\chi_4^0)$:	three-particle edge($\chi_4^0, \tilde{l}_R, \chi_1^0$)	254.29	3.3	0.3		4.1
$m_{\tau\tau}^{\max}$:	three-particle edge($\chi_2^0, \tilde{\tau}_1, \chi_1^0$)	83.27	5.0		0.8	2.1
m_{lq}^{high} :	four-particle edge($\tilde{q}_L, \chi_2^0, \tilde{l}_R, \chi_1^0$)	390.28	1.4		3.8	13.9
m_{llq}^{thres} :	threshold($\tilde{q}_L, \chi_2^0, \tilde{l}_R, \chi_1^0$)	216.22	2.3		2.0	8.7
m_{llb}^{thres} :	threshold($\tilde{b}_1, \chi_2^0, \tilde{l}_R, \chi_1^0$)	198.63	5.1		1.8	8.0

Table 4.4: LHC measurements in SPS1a, taken from [46]. Shown are the nominal values (from SuSpect) and statistical errors, systematic errors from the lepton (LES) and jet energy scale (JES) and theoretical errors. All values are given in GeV. Table taken from [35].

For the ILC, as a rule of thumb, if particles are light enough to be produced in pairs given the center-of-mass energy of the collider, their mass can be determined with an order of magnitude better precision. Two separate methods provide mass measurements. Direct reconstruction, i.e., for the observed decay products of the sparticles in the detector relies on the precision of the energy scale of the detector. The second method, a counting experiment, is based on the measurement of the cross section as function of the (variable) center-of-mass energy of the ILC. Here, experimentally, the precise determination of the beam energy is of the utmost importance, whereas the challenge for the detector data is the understanding of the efficiency. Both methods have comparable precision in the per mil region, but different systematical errors. Additionally discrete quantum numbers like the spin of the particles can be determined as well by the analysis of the angular distributions.

	m_{SPS1a}	LHC	ILC	LHC+ILC		m_{SPS1a}	LHC	ILC	LHC+ILC
h	108.99	0.25	0.05	0.05	H	393.69		1.5	1.5
A	393.26		1.5	1.5	$H+$	401.88		1.5	1.5
χ_1^0	97.21	4.8	0.05	0.05	χ_2^0	180.50	4.7	1.2	0.08
χ_3^0	356.01		4.0	4.0	χ_4^0	375.59	5.1	4.0	2.3
χ_1^\pm	179.85		0.55	0.55	χ_2^\pm	375.72		3.0	3.0
\tilde{g}	607.81	8.0		6.5					
\tilde{t}_1	399.10		2.0	2.0	\tilde{b}_2	544.85	7.9		6.2
\tilde{b}_1	518.87	7.5		5.7	\tilde{q}_R	543.82	9.5		8.0
\tilde{q}_L	562.98	8.7		4.9	\tilde{e}_R	142.65	4.8	0.05	0.05
\tilde{e}_L	199.66	5.0	0.2	0.2	$\tilde{\mu}_R$	142.65	4.8	0.2	0.2
$\tilde{\mu}_L$	199.66	5.0	0.5	0.5	$\tilde{\tau}_2$	203.69		1.1	1.1
$\tilde{\tau}_1$	133.35	6.5	0.3	0.3					
$\tilde{\nu}_e$	183.79		1.2	1.2					

Table 4.5: Errors for the mass determination in SPS1a, taken from [46]. Shown are the nominal parameter values (from SuSpect), the error for the LHC alone, from the ILC alone, and from a combined LHC+ILC analysis (taken from [35])

The summary of particle mass measurements is listed in Table 4.5, taken from Ref. [35]. The central values are calculated by SuSpect [62]. The coverage of the LHC is better in the strongly interacting sector, whereas the ILC has the advantage of higher precision in the gaugino/slepton sector [90, 91, 92, 93]. As pointed out in Ref. [73, 74], the use of the ILC measurement of the LSP in the kinematic determination of the squark masses increases their precision.

4.3 Treatment of Errors

A rigorous treatment of the errors is essential to obtain the most precise and also reliable estimation of the fundamental parameters. There are three different sources of errors: experimental statistical errors, experimental systematic errors and theoretical errors. Systematic errors can have different sources, such as the energy scale or the knowledge of the efficiency and varying degrees of correlation. The picture even depends on the measurements used in the analysis: edges and thresholds have independent statistical errors

and correlated energy scale errors, but when translating them into masses, the masses are then non-trivially correlated. Theoretical errors are an estimate of unknown higher order corrections.

In SFitter the CKMfitter prescription for the RFit scheme [94, 95] is followed. The experimental errors are treated as Gaussian and the full correlation matrix is included. The theoretical errors are flat errors. Therefore any central value within the range is equally probable. This description is particularly well adapted as the error covers also missing higher order calculations. In this case the higher order, once it is calculated, should move the central value of the prediction within the error. This behavior would be contrary to the Gaussian expectation.

While in the supersymmetric measurements the errors are essentially Gaussian, for the study of the Higgs parameters, low counting rates (after background subtraction) are expected. A combination scheme of Poisson and Gaussian errors was developed under the guiding principle that in the Gaussian limit the formula should simplify to the quadratic sum of the errors. The detailed procedure is described in the Appendix of [36].

The contribution to the χ^2 of a given measurement is zero within 1σ of the theoretical error and outside of this range the experimental error is used. Given a set of measurements \vec{d} and a general correlation matrix C

$$\chi^2 = \vec{\chi}_d^T C^{-1} \vec{\chi}_d$$

$$|\chi_{d,i}| = \begin{cases} 0 & |d_i - \bar{d}_i| < \sigma_i^{(\text{theo})} \\ \frac{|d_i - \bar{d}_i| - \sigma_i^{(\text{theo})}}{\sigma_i^{(\text{exp})}} & |d_i - \bar{d}_i| > \sigma_i^{(\text{theo})} \end{cases}, \quad (4.2)$$

where \bar{d}_i is the i -th data point predicted by the model parameters and d_i the measurement.

A complication with flat distributions is that in the central region the log-likelihood can be constant as a function of model parameters. In those regions these parameters vanish from the counting of degrees of freedom.

To determine the errors on the fundamental parameters, two techniques are used: a direct determination for the best fit using MINUIT and using sets of toy measurements. The advantage of MINUIT is that only one fit is necessary to determine the errors, but the presence of correlations and the flat theory errors complicate the error determination. The toy experiments method is used by SFitter unless stated otherwise. The search for the best-fit

point is performed several (10000) times. The datasets are smeared according to the experimental and theoretical errors including the correlations among them.

4.4 Measuring mSUGRA

Determining the parameters from a given set of measurements necessitates efficient algorithms. The determination of the mSUGRA parameters can be used as an illustrative example. Four parameters have to be determined and one sign. The smuon mass depends on m_0 and $m_{1/2}$, the neutralino mass depends on $\tan\beta$ and $m_{1/2}$, among others. The measurements are strongly correlated, e.g., via the energy scale error.

4.4.1 Determination of the True Central Value

The first question to be asked is whether the correct parameter set can be found. Thus the algorithm has to be able to disentangle the different contributions. The simplest approach is to use a gradient fit, i.e., MINUIT. In a tightly constrained system such as mSUGRA this is sufficient to find the correct parameter set even if the starting values for the parameters are far from the true SPS1a values. The sign of the μ parameter is then determined by the quality of the fit: performing the fit with the wrong sign of μ leads to larger χ^2 value than the correct sign of μ .

However, the result could depend on the starting point when the fit remains confined to a secondary minima by a “potential” wall in χ^2 . Simulated annealing was developed in Ref. [75] to allow to escape the secondary minimum and find the correct solution. In SFitter weighted Markov chains were developed. Markov chains are linear in the number of parameters, an important property for the determination of the MSSM parameters, and are capable of finding secondary minima.

First, fully exclusive log-likelihood maps are calculated. From these different types of projections are possible: Bayesian or frequentist (profile likelihood). Successive projections over unwanted parameters allow to study the correlations between parameters. In the Bayesian approach a measure, the Bayesian prior, is introduced and the parameter is integrated over. In the frequentist approach the parameter value of the minimum χ^2 (maximum likelihood) is retained. The Bayesian approach ensures that after the pro-

jection the distributions have the quality of a probability density function. The advantage of the frequentist approach is that the absolute minimum is always retained, however the pdf property is lost.

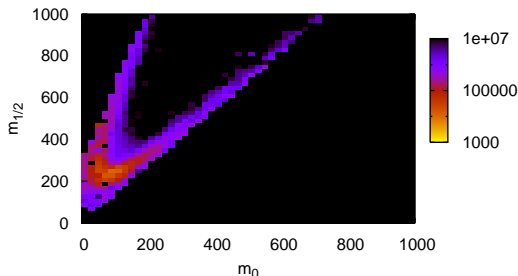


Figure 4.5: m_0 - $m_{1/2}$ plane of SPS1a for LHC measurements after the Bayesian projection (from [35]).

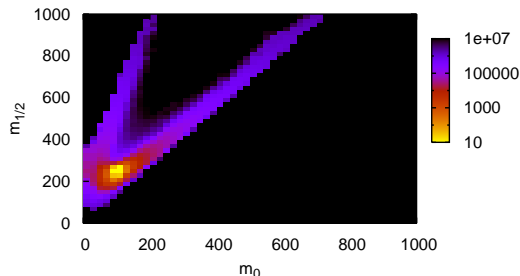


Figure 4.6: m_0 - $m_{1/2}$ plane of SPS1a for LHC measurements after the frequentist projection (from [35]).

An example is shown in Figure 4.5 for the Bayesian approach with a flat prior and in Figure 4.6 for the frequentist approach in the m_0 - $m_{1/2}$ plane of SPS1a for LHC measurements. While the general structure is similar and the correct parameters were determined, due to the definition of the frequentist projection the best-fit is brighter. In the Bayesian case the sharp maximum/minimum is washed out by the integration over large regions with small likelihood (noise effect). One can also see the parabolic correlation between the parameters as expected from, e.g., the sfermion masses.

χ^2	m_0	$m_{1/2}$	$\tan \beta$	A_0	μ	m_t
0.09	102.0	254.0	11.5	-95.2	+	172.4
1.50	104.8	242.1	12.9	-174.4	-	172.3
73.2	108.1	266.4	14.6	742.4	+	173.7
139.5	112.1	261.0	18.0	632.6	-	173.0
...						

Table 4.6: List of minima found in mSUGRA for the LHC measurements (taken from [35]).

The expected error on the top quark mass measurement is $1 \text{ GeV}/c^2$ at the LHC and an order of magnitude more precise at the ILC ($0.12 \text{ GeV}/c^2$). The top quark mass therefore has a double role, it is a parameter of the model [96, 97, 98, 84] which can have a large impact on the prediction of masses such as the Higgs boson mass [99, 100, 101]. The top quark mass is also treated

as a measurement with the appropriate error in the determination of the parameters. In principal all Standard Model parameters would need to be treated this way, however, the impact is practically negligible for the other parameters, so that they can be fixed to the central value. An exception is the b-quark mass for high $\tan\beta$ regions.

The list of secondary minima for the LHC measurements is shown in Table 4.6, including the top quark mass as a parameter. Even in such a tightly constrained model with a small number of parameters secondary minima can be observed in addition to the correct parameter point (first line of Table 4.6). It is particularly interesting to note that the addition of the top quark mass as a parameter adds a secondary minimum (third line) in its interplay with trilinear coupling. However, all secondary minima can easily be eliminated by the absolute value of the χ^2 which is higher than for the correct SPS1a parameter set. A dataset which was smeared according to the expected errors, including all correlations, was used for this determination. Therefore a small shift in the parameters is expected as the dataset does not correspond to the true value of SPS1a.

4.4.2 Determining the Errors on the Parameters

The second question is to determine the precision with which the parameters can be determined. At this point the theoretical errors have to be specified. The Higgs boson mass prediction is known with a precision of $3\text{GeV}/c^2$. Strongly interacting particles such as squarks and gluinos have an error of 3%. Electromagnetically and weakly interacting particles such as neutralinos and sleptons have an uncertainty of 1% of their mass prediction [91, 92, 93]. The errors defined on the masses were propagated to the edges and thresholds.

At the LHC, one has the choice to either use the edges and thresholds directly or the masses derived from the edges and thresholds [106, 107, 108, 109]. A comparison of the expected precision is shown in Table 4.7. The precision is improved by the use of edges and thresholds instead of the masses. In fact, the determination of the mass introduces non-negligible correlations among them. As these correlations are not available, there is a loss of information which translates into a less precise determination of the fundamental parameters by a factor of between two and three for m_0 and $m_{1/2}$. Further evidence for the impact of correlations is seen by the improvement of the error on m_0 when the correlation of the lepton and jet energy scale errors are taken into account.

	SPS1a	$\Delta_{\text{zero}}^{\text{theo-exp}}$	$\Delta_{\text{zero}}^{\text{expNoCorr}}$	$\Delta_{\text{zero}}^{\text{theo-exp}}$	$\Delta_{\text{gauss}}^{\text{theo-exp}}$	$\Delta_{\text{flat}}^{\text{theo-exp}}$
		masses		endpoints		
m_0	100	4.11	1.08	0.50	2.97	2.17
$m_{1/2}$	250	1.81	0.98	0.73	2.99	2.64
$\tan \beta$	10	1.69	0.87	0.65	3.36	2.45
A_0	-100	36.2	23.3	21.2	51.5	49.6
m_t	171.4	0.94	0.79	0.26	0.89	0.97

Table 4.7: Errors on the parameter determination at the LHC in SPS1a. The big columns are mass and endpoint measurements. The subscript represents neglected, (probably approximate) Gaussian or flat theory errors. The experimental error includes correlations unless indicated otherwise in the superscript (taken from [35]).

Theory errors have an impact on the determination of the parameters at the LHC. As shown in Table 4.7, the proper inclusion of theory errors as flat errors reduces the LHC precision significantly. An example is the Higgs boson mass which is sensitive to $\tan \beta$, but its theoretical error is an order of magnitude worse than the expected experimental error.

Theoretical errors not only parametrize not-yet calculated high order corrections but also variations of results between calculations at the same order. As a check of the consistency of the theory errors, the SPS1a spectrum calculated by SoftSUSY was fitted with SuSpect. While the parameter central values were shifted, they were within 3σ of the correct ones adding confidence in the theory errors.

The table of measurements at the LHC hides a part of the complexity of the determination of the parameters: three neutralinos are observed, the third lightest, due to Higgsino nature is not. Therefore one has to be able to infer from the data which of the neutralinos were observed. The most difficult example is to wrongly label the measurement of the fourth neutralino as third. A parameter determination can be performed and m_0 and $m_{1/2}$ are off by up to $1 \text{ GeV}/c^2$. The χ^2 value of the fit remains reasonable. While this looks like a true difficult secondary minimum, the parameters determined can be used to predict the spectrum, production cross section and branching ratios. Analyzing these results, a larger production of χ_4^0 than χ_3^0 is expected in disagreement to the labeling, discarding effectively this secondary minimum. It is clear that a lot of thought has to go into the definition of the table of observables to make sure that all underlying/hidden assumptions are tested.

An automated algorithm for all does not seem feasible.

	SPS1a	$\Delta_{\text{endpoints}}$	Δ_{ILC}	$\Delta_{\text{LHC+ILC}}$	$\Delta_{\text{endpoints}}$	Δ_{ILC}	$\Delta_{\text{LHC+ILC}}$
		exp. errors			exp. and theo. errors		
m_0	100	0.50	0.18	0.13	2.17	0.71	0.58
$m_{1/2}$	250	0.73	0.14	0.11	2.64	0.66	0.59
$\tan\beta$	10	0.65	0.14	0.14	2.45	0.35	0.34
A_0	-100	21.2	5.8	5.2	49.6	12.0	11.3
m_t	171.4	0.26	0.12	0.12	0.97	0.12	0.12

Table 4.8: Expected errors for mSUGRA at the LHC (endpoints) and ILC. Only absolute errors are given. Flat theory errors are used (taken from [35]).

The ILC will start taking data after the LHC has taken data and discovered SPS1a (if nature is kind enough). The added value of the ILC is the completion of the particle spectrum and the measurement of all particles with an impressive accuracy, about an order of magnitude improved on the LHC. The results are shown in Table 4.8. The precision improvement by the ILC per se is about a factor of five. The improvement of the combination LHC and ILC over ILC alone is rather marginal. Comparing the LHC+ILC errors with and without theory errors shows the margin for the improvement of theory predictions, as shown already for the LHC, justifying the SPA project [43]. The SPA project’s goal is to improve the theory predictions for the supersymmetry (S) parameter (P) analysis (A).

4.5 Measuring the MSSM

mSUGRA has the advantage of being a model with few parameters which is mostly defined at the GUT scale. The unification of breaking parameters at the GUT scale is assumed. The MSSM, defined at the electroweak scale, allows to measure grand unification without imposing it. The MSSM parameter determination is far more difficult technically: more parameters have to be determined from the same dataset. The reward is to be able to extrapolate the MSSM parameters to the GUT scale and thus measure grand unification or other models such as GMSB.

	$\mu < 0$				$\mu > 0$			
					SPS1a			
M_1	96.6	175.1	103.5	365.8	98.3	176.4	105.9	365.3
M_2	181.2	98.4	350.0	130.9	187.5	103.9	348.4	137.8
μ	-354.1	-357.6	-177.7	-159.9	347.8	352.6	178.0	161.5
$\tan \beta$	14.6	14.5	29.1	32.1	15.0	14.8	29.2	32.1
M_3	583.2	583.3	583.3	583.5	583.1	583.1	583.3	583.4
$M_{\tilde{\tau}_L}$	114.9	2704.3	128.3	4794.2	128.0	229.9	3269.3	118.6
$M_{\tilde{\tau}_R}$	348.8	129.9	1292.7	130.1	2266.5	138.5	129.9	255.1
$M_{\tilde{\mu}_L}$	192.7	192.7	192.7	192.9	192.6	192.6	192.7	192.8
$M_{\tilde{\mu}_R}$	131.1	131.1	131.1	131.3	131.0	131.0	131.1	131.2
$M_{\tilde{e}_L}$	186.3	186.4	186.4	186.5	186.2	186.2	186.4	186.4
$M_{\tilde{e}_R}$	131.5	131.5	131.6	131.7	131.4	131.4	131.5	131.6
$M_{\tilde{q}^3_L}$	497.1	497.2	494.1	494.0	495.6	495.6	495.8	495.0
$M_{\tilde{t}_R}$	1073.9	920.3	547.9	950.8	547.9	460.5	978.2	520.0
$M_{\tilde{b}_R}$	497.3	497.3	500.4	500.9	498.5	498.5	498.7	499.6
$M_{\tilde{q}_L}$	525.1	525.2	525.3	525.5	525.0	525.0	525.2	525.3
$M_{\tilde{q}_R}$	511.3	511.3	511.4	511.5	511.2	511.2	511.4	511.5
$A_t (-)$	-252.3	-348.4	-477.1	-259.0	-470.0	-484.3	-243.4	-465.7
$A_t (+)$	384.9	481.8	641.5	432.5	739.2	774.7	440.5	656.9
m_A	350.3	725.8	263.1	1020.0	171.6	156.5	897.6	256.1
m_t	171.4	171.4	171.4	171.4	171.4	171.4	171.4	171.4

Table 4.9: Eight best-fitting points in the MSSM with two alternative solutions for A_t . The χ^2 value for all points is approximately the same, so the ordering of the table is arbitrary. The parameter point closest to the correct point is labeled as SPS1a (taken from [35]).

4.5.1 Determination of the True Central Value

The problem of the higher-dimensional MSSM parameter space with respect to the mSUGRA case is solved by a combination of techniques (for details see [35]). In particular a sequence of Markov chains and gradient fits is used. A second Markov chain step combined with the gradient fit is performed in the gaugino–Higgsino subspace and the other parameters are re-determined subsequently. This complex procedure leads to the identification of the primary minimum/maximum and an eightfold ambiguity listed in Table 4.9. Additionally, alternative likelihood maxima are triggered by correlations between the rather poorly measured parameters A_t , $\tan \beta$ and the right-handed stop mass.

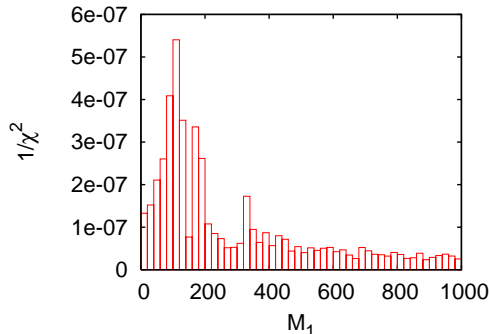


Figure 4.7: The Bayesian projection for M_1 is shown for LHC data [35]).

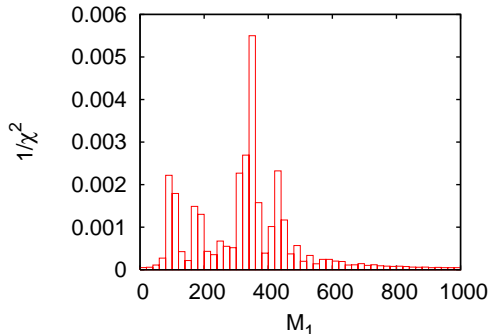


Figure 4.8: The profile likelihood for M_1 is shown for LHC data [35]).

Solutions are observed for the two signs of μ and for each sign of μ four solutions are determined, two of which can be grouped together by interchanging M_1 and M_2 . The correct solution differs from the nominal values of SPS1a as a smeared dataset was used for this study. In Figure 4.7 the Bayesian projection is shown and in Figure 4.8 the frequentist projection is shown. While in the Bayesian projection the central values are washed out by noise effects, the profile likelihood allows to identify the location of the ambiguities.

4.5.2 Determining the Errors

In principle 22 measurements are available at the LHC, thus technically enough to determine the 19 parameters of the MSSM (including the top

quark mass as a parameter). However, these measurements come from only 15 different masses. Therefore, inevitably, some parameters must be fixed in order to determine the errors with no impact on the determination as these parameters have essentially a very weak impact on the observables. The result is shown in Table 4.10 including flat theory errors.

The stau sector is inevitably poorly determined at the LHC as only one measurement is available for the parameters. The stop sector (no measurements in SPS1a) can only be determined indirectly with a penalty paid in the size of the error. For the ILC several parameters have to be fixed as the strongly interacting particles such as squarks and gluinos with the exception of the lightest stop cannot be produced. The historical motivation for fixing the squark parameters in the ILC study was the possibility of concurrent running of LHC and ILC. As this is no longer an option the more realistic scenario will be that the parameters for the ILC-alone study will be fixed to the measurements of the LHC. The fixed parameters in the ILC column of Table 4.10 are within 5%-15% of such a scenario. The main impact of the combination of LHC and ILC is observed in the last column of Table 4.10, where all parameters can be determined, with the exception of the tri-linear couplings of the first two generation, which have no effect on the observables in the selectron and smuon sector.

Comparing the effect of taking into account the theoretical errors, about a factor five in precision is lost with today's calculations at the ILC. Its precision is decreased from per mil to 0.5%. For the LHC roughly a factor two is lost. The combination of LHC and ILC measurements can be particularly useful to determine the link to dark-matter observables [79, 122, 123, 124, 125, 76, 126, 127, 128].

4.5.3 Extrapolating to the GUT Scale

Once the parameters of the weak-scale MSSM-Lagrangian have been determined, the next step is to extrapolate the parameters all the way to the Planck scale. Inspired by the apparent unification of the gauge couplings [17] in the MSSM the question arises if any other running parameters unify at a higher scale, as shown in the pioneering work in [73, 74].

Technically, upwards running is considerably more complicated [129] than starting from a unification-scale and testing the unification hypothesis by comparing to the weak-scale particle spectrum. For example, it is not guaranteed that the renormalization group running will converge for weak-scale

	LHC		ILC		LHC+ILC		SPS1a
$\tan\beta$	$10.0\pm$	4.5	$12.1\pm$	7.0	$12.6\pm$	6.2	10.0
M_1	$102.1\pm$	7.8	$103.3\pm$	1.1	$103.2\pm$	0.95	103.1
M_2	$193.3\pm$	7.8	$194.1\pm$	3.3	$193.3\pm$	2.6	192.9
M_3	$577.2\pm$	14.5	fixed 500		$581.0\pm$	15.1	577.9
$M_{\tilde{\tau}_L}$	$227.8\pm\mathcal{O}(10^3)$		$190.7\pm$	9.1	$190.3\pm$	9.8	193.6
$M_{\tilde{\tau}_R}$	$164.1\pm\mathcal{O}(10^3)$		$136.1\pm$	10.3	$136.5\pm$	11.1	133.4
$M_{\tilde{\mu}_L}$	$193.2\pm$	8.8	$194.5\pm$	1.3	$194.5\pm$	1.2	194.4
$M_{\tilde{\mu}_R}$	$135.0\pm$	8.3	$135.9\pm$	0.87	$136.0\pm$	0.79	135.8
$M_{\tilde{e}_L}$	$193.3\pm$	8.8	$194.4\pm$	0.91	$194.4\pm$	0.84	194.4
$M_{\tilde{e}_R}$	$135.0\pm$	8.3	$135.8\pm$	0.82	$135.9\pm$	0.73	135.8
$M_{\tilde{q}^3_L}$	$481.4\pm$	22.0	$499.4\pm$	$\mathcal{O}(10^2)$	$493.1\pm$	23.2	480.8
$M_{\tilde{t}_R}$	$415.8\pm\mathcal{O}(10^2)$		$434.7\pm\mathcal{O}(4\cdot 10^2)$		$412.7\pm$	63.2	408.3
$M_{\tilde{b}_R}$	$501.7\pm$	17.9	fixed 500		$502.4\pm$	23.8	502.9
$M_{\tilde{q}_L}$	$524.6\pm$	14.5	fixed 500		$526.1\pm$	7.2	526.6
$M_{\tilde{q}_R}$	$507.3\pm$	17.5	fixed 500		$509.0\pm$	19.2	508.1
A_τ	fixed 0		$613.4\pm$	$\mathcal{O}(10^4)$	$764.7\pm\mathcal{O}(10^4)$		-249.4
A_t	$-509.1\pm$	86.7	$-524.1\pm$	$\mathcal{O}(10^3)$	$-493.1\pm$	262.9	-490.9
A_b	fixed 0		fixed 0		$199.6\pm\mathcal{O}(10^4)$		-763.4
$A_{l1,2}$	fixed 0		fixed 0		fixed 0		-251.1
$A_{u1,2}$	fixed 0		fixed 0		fixed 0		-657.2
$A_{d1,2}$	fixed 0		fixed 0		fixed 0		-821.8
m_A	$406.3\pm\mathcal{O}(10^3)$		$393.8\pm$	1.6	$393.7\pm$	1.6	394.9
μ	$350.5\pm$	14.5	$354.8\pm$	3.1	$354.7\pm$	3.0	353.7
m_t	$171.4\pm$	1.0	$171.4\pm$	0.12	$171.4\pm$	0.12	171.4

Table 4.10: Results for the general MSSM parameter determination in SPS1a using flat theory errors. The kinematic endpoint measurements are used for the LHC and the mass measurements for the ILC. The LHC+ILC column is the combination of the two measurements sets. Shown are the nominal parameter values and the result after fits to the different data sets (taken from [35]).

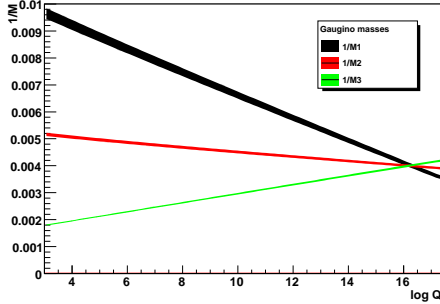


Figure 4.9: Extrapolation of the inverse of the gaugino mass parameters to the GUT scale for the correct solution at the LHC.

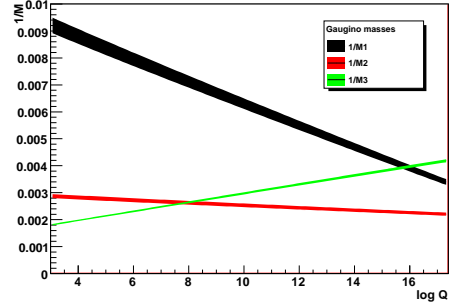


Figure 4.10: Extrapolation of the inverse of the gaugino mass parameters to the GUT scale for a false solution at the LHC.

input values far away from the top-down prediction.

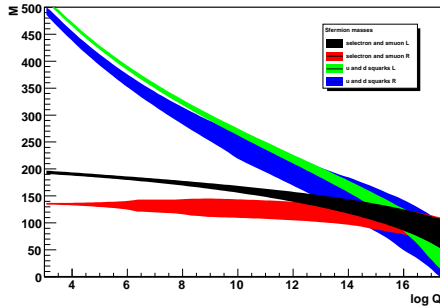


Figure 4.11: Extrapolation of the first and second generation scalar mass parameters to the GUT scale for the correct solution at the LHC.

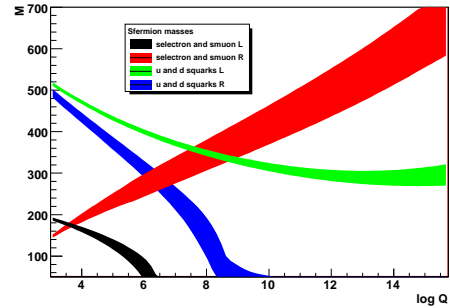


Figure 4.12: Extrapolation of the first and second generation scalar mass parameters to the GUT scale for a false solution at the LHC.

The first step in the extrapolation of the weak scale parameters is to test the expected measurement of the gaugino mass parameters at the LHC. Figure 4.9 shows the result for the true parameter point. In Figure 4.10 the extrapolation is performed for one of the ambiguous solutions. While grand unification is observed for the correct parameter set as expected, in the second case unification is not observed. The non-unification of six of the solutions is easy to observe. The seventh solution shows a close miss of unification. It will therefore depend on the exact precision of the LHC measurement whether it can be distinguished from the correct solution which unifies the parameters

at the GUT scale.

For the extrapolation of the scalar mass parameters at the LHC alone the picture is even more difficult. In Figure 4.11 the unification of the first and second generation scalar mass parameters is observed for the correct solution, however in Figure 4.12 the stau parameters have been moved to different values. This behavior can be understood from the RGEs. In the gaugino sector the RGEs do not depend on other parameters. In the scalar sector the RGEs are strongly coupled, so that a wrong value of a stau parameter can wreak havoc in the extrapolation of the first and second generation scalar parameters.

If no further measurements are thought of for the SPS1a scenario, the proof and measurement of grand unification of supersymmetric parameters will have to wait until the ILC resolves the ambiguities. With the ILC a unique solution of the MSSM parameters is determined, which can then be extrapolated to truly measure grand unification of the supersymmetric breaking parameters as shown in Chapter 5.

4.6 Measuring the Higgs Sector

A more difficult scenario at the LHC would be to discover only a Higgs boson in two-particle decays. The question arises naturally if there is more to learn from this sector than the Higgs boson mass, which is used also in the supersymmetric parameter determination. In analogy to the measurement of the Triple Gauge Couplings (TGC) at LEP, one can parametrize the Higgs couplings as deviation from the Standard Model expectation.

Thus a tree-level Standard Model Higgs coupling to any particle j is defined as:

$$g_{jjH} \longrightarrow g_{jjH}^{\text{SM}} (1 + \Delta_{jjH}) \quad (4.3)$$

where the Δ_{jjH} are independent of each other. The three loop induced couplings in the Higgs sector, g_{ggH} , $g_{\gamma\gamma H}$ and $g_{\gamma ZH}$, sensitive to new physics [172, 173, 174, 175], are defined in the following way:

$$g_{jjH} \longrightarrow g_{jjH}^{\text{SM}} (1 + \Delta_{jjH}^{\text{tree}} + \Delta_{jjH}) \quad (4.4)$$

where g_{jjH}^{SM} is the loop-induced coupling in the Standard Model, $\Delta_{jjH}^{\text{tree}}$ is the contribution from modified tree-level couplings to Standard-Model particles (in the loop), Δ_{jjH} is an additional contribution proper for this effective coupling.

In the scenario treated in this analysis, a Higgs boson mass of $120 \text{ GeV}/c^2$, the total width is defined as the sum of the measured partial widths. As the partial width of the decay Higgs to bb is 90% of the total width, it is measured reasonably well at the LHC.

The total width can be varied just like the couplings

$$\Gamma_{\text{tot}} = \Gamma_{\text{tot}}^{\text{SM}} (1 + \Delta\Gamma) \quad . \quad (4.5)$$

This parameter can be used of an unobserved channel/anomalous channel.

4.6.1 Determination of the True Couplings

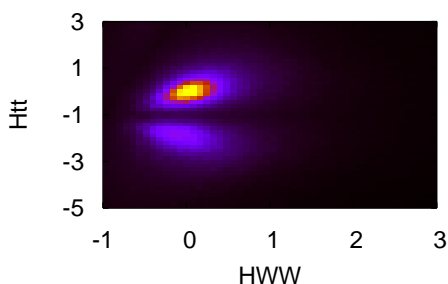


Figure 4.13: Profile likelihood for the ttH and WWH couplings for 30 fb^{-1} (from [36]).

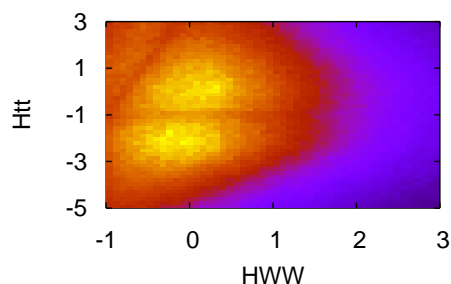


Figure 4.14: Bayesian projection for the ttH and WWH couplings for 30 fb^{-1} (from [36]).

The procedure for the determination of the Higgs boson couplings follows the strategy applied in the determination of the supersymmetric couplings. An exclusive likelihood map is calculated for the parameters ΔjjH , the deviations from the Standard Model couplings. From this map different projections are possible to study correlations.

The analysis is performed for an integrated luminosity of 30 fb^{-1} . The errors cannot be scaled simply to 300 fb^{-1} since e.g., the systematic error on the mini-jet veto for nominal LHC luminosity is not known. The first parameter set used for the true dataset (without smearing) are the tree-level couplings: WWH , ZZH , ttH , $\tau\tau H$ and no genuine anomalous contribution to the effective couplings is allowed. The overall phase of the couplings is fixed by requiring WWH to be positive without loss of generality.

While in the supersymmetric case genuine secondary minima can arise, e.g., particularly in the MSSM, in the Higgs couplings no such effect is expected. In fact, the definition of the parameters leads to quadratic dependence of the observables on the parameters.

The Bayesian projection is shown in Figure 4.13 and the frequentist approach of maintaining always the absolute minimum/maximum is shown in Figure 4.14. From the comparison of the two figures one can conclude that the important integration (noise) effect renders the Bayesian approach less performant than the profile likelihood.

The profile likelihood in Figure 4.14 shows a well identified correct solution. It is interesting to note that in spite of the observables being essentially quadratic in the parameters, a clear preference for the correct solution is observed for H_{tt} . The reason is that the rate of Higgs to two photons is sensitive to the relative sign.

In general, a positive correlation among the couplings is observed among the couplings induced by the general ($\sigma \cdot \text{BR}$) structure of the LHC measurements. A change in the bbH coupling will induce a coherent compensation on the production side and decay side of the observables as the total width in the denominator is dominated by the bbH partial width.

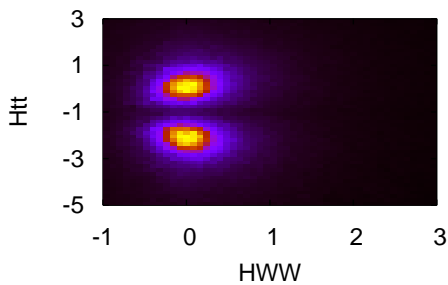


Figure 4.15: Profile likelihoods for WWH versus ttH allowing genuine contributions to the effective couplings (taken from [36]).

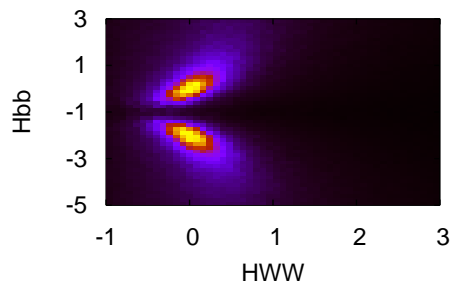


Figure 4.16: Profile likelihoods for WWH versus bbH allowing genuine contributions to the effective couplings (taken from [36]).

In Figure 4.15 and Figure 4.16 the correlations of the WWH with the ttH and bbH couplings are shown. Here the effective couplings are left free and are part of the parameter set to be determined. The general feature of a positive correlation is still observed, especially clear for the bbH versus

WWH coupling. However, the sign sensitivity of the $\gamma\gamma$ channel is lost due to the additional freedom added by the effective anomalous couplings.

While these results seem to indicate that the absolute couplings of the Higgs boson can be determined at the LHC, a simple scenario shows that this is not the case. In the studies discussed above, the ccH coupling was fixed to its Standard Model value. What would be the effect of a large anomalous ccH coupling? The observed rates would be diminished by Γ_H/Γ_{H+ccH} . In the coupling determination the anomalous couplings would deviate from the Standard Model value and be negative. This situation is thus indistinguishable from genuine anomalous couplings.

In practice the coherent observation of the reduction of all couplings would lead to a study of the Δ_Γ parameter. This parameter is determined in a single parameter fit. It cannot be determined in a global fit including the anomalous Higgs couplings due to the structure of the observables (blind direction).

Absolute coupling measurements at the LHC therefore depend on the (additional) assumptions to be made in contrast to coupling ratios. A model independent study will have to wait for the ILC.

4.6.2 Error determination

	no effective couplings				with effective couplings			
	RMS	σ_{symm}	σ_{neg}	σ_{pos}	RMS	σ_{symm}	σ_{neg}	σ_{pos}
m_H	± 0.36	± 0.26	-0.26	$+0.26$	± 0.38	± 0.25	-0.26	$+0.25$
Δ_{WWH}	± 0.31	± 0.23	-0.21	$+0.26$	± 0.29	± 0.24	-0.21	$+0.27$
Δ_{ZZH}	± 0.49	± 0.36	-0.40	$+0.35$	± 0.46	± 0.31	-0.35	$+0.29$
$\Delta_{t\bar{t}H}$	± 0.58	± 0.41	-0.37	$+0.45$	± 0.59	± 0.53	-0.65	$+0.43$
$\Delta_{b\bar{b}H}$	± 0.53	± 0.45	-0.33	$+0.56$	± 0.64	± 0.44	-0.30	$+0.59$
$\Delta_{\tau\bar{\tau}H}$	± 0.47	± 0.33	-0.21	$+0.46$	± 0.57	± 0.31	-0.19	$+0.46$
$\Delta_{\gamma\gamma H}$	—	—	—	—	± 0.55	± 0.31	-0.30	$+0.33$
Δ_{ggH}	—	—	—	—	± 0.80	± 0.61	-0.59	$+0.62$
m_b	± 0.073	± 0.071	-0.071	$+0.071$	± 0.070	± 0.071	-0.071	$+0.072$
m_t	± 1.99	± 1.00	-1.03	$+0.98$	± 1.99	± 0.99	-1.00	$+0.98$

Table 4.11: Errors on the measurements from 10000 toy experiments for an integrated luminosity of 30 fb^{-1} (taken from [36]).

The errors on the Higgs boson couplings are determined with 10000 toy datasets. The datasets were smeared according to the experimental and

theoretical errors, including the correlations among them. The results are shown in Table 4.11 without and with anomalous effective couplings.

The RMS is shown, as well as the fit of a symmetric Gaussian and the fit of two separate Gaussian for the positive and negative side of the coupling. The expected precision for the coupling measurement is typically between 25% and 45%. As statistics increase (higher luminosity) the difference between RMS and the Gaussian fits should decrease.

Adding the effective couplings to the parameter sets, one would expect an increase of the errors. While this is true in most cases, e.g., the ZZH coupling is decreased. One can understand this effect by the impact of correlations. The rate of the ZZ final state is the upper limit. With a positive correlation between the effective coupling (production side) and the HZZ (decay side), the effective values that the ZZH coupling can take on are actually reduced, leading to a smaller error.

	no effective couplings			with effective couplings		
	σ_{symm}	σ_{neg}	σ_{pos}	σ_{symm}	σ_{neg}	σ_{pos}
$\Delta_{ZZH}/\Delta_{WWH}$	± 0.46	-0.36	$+0.53$	± 0.41	-0.40	$+0.41$
$\Delta_{t\bar{t}H}/\Delta_{WWH}$	± 0.30	-0.27	$+0.32$	± 0.51	-0.54	$+0.48$
$\Delta_{b\bar{b}H}/\Delta_{WWH}$	± 0.28	-0.24	$+0.32$	± 0.31	-0.24	$+0.38$
$\Delta_{\tau\bar{\tau}H}/\Delta_{WWH}$	± 0.25	-0.18	$+0.33$	± 0.28	-0.16	$+0.40$
$\Delta_{\gamma\gamma H}/\Delta_{WWH}$	—	—	—	± 0.30	-0.27	$+0.33$
$\Delta_{ggH}/\Delta_{WWH}$	—	—	—	± 0.61	-0.71	$+0.46$

Table 4.12: Errors on the ratio of couplings, corresponding to Table 4.11 (taken from [36]).

The errors on the ratios are shown in Table 4.12. As many experimental and theoretical errors are correlated, one would expect that the ratios are measured more precisely than the absolute couplings. However the effect is relatively small. This is essentially due to the statistics of the signal for 30 fb^{-1} . For the experimental error the statistical error is much larger than the systematic error which is canceled in the ratio. The definition of the flat errors implies that outside the theoretical errors, the χ^2 varies only with the experimental error. As the experimental error is much larger, the theoretical errors do not have a large impact. This has been checked by removing the theoretical errors entirely, which has only a marginal effect.

To illustrate the importance of the measurement of the bbH coupling, in Figure 4.17 the effect of the subjet analysis is shown with full sensitivity, re-

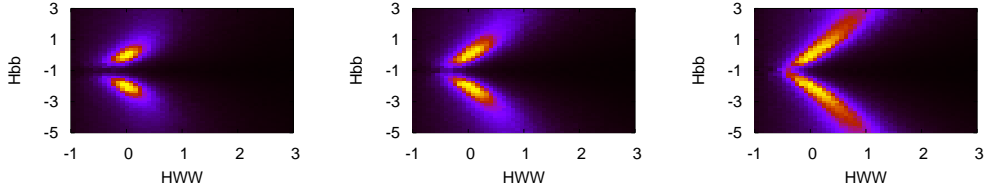


Figure 4.17: Impact of the subjet analysis. The sensitivity is 100% (left), 50% (middle) and entirely removed (right) (taken from [36]).

ducing its sensitivity by 50% and removing it entirely. ATLAS has confirmed the theoretical study within recently 10%, i.e., 3.7σ significance versus 4.2σ which is closest to the full sensitivity in Figure 4.17.

4.6.3 Supersymmetric Higgs Scenarios

In the favorable case of low mass supersymmetry, supersymmetric particles will be discovered well before the lightest Higgs boson. However, there are scenarios where the supersymmetric particles are out of reach or need very high integrated luminosity to be discovered and the Standard Model Higgs boson is the first “supersymmetric” particle discovered. In such a case it is interesting to ask whether the measurement of the Higgs boson couplings could be used to probe new physics in the absence of/or ignoring direct evidence.

Two scenarios were studied in [36] of which only one will be discussed here as an illustration. The parameter set is a modified version of SPS1a. The study is based on the assumption that only a Higgs boson has been measured with a mass of $120 \text{ GeV}/c^2$ and no supersymmetric measurements have been made.

	Δ_{WWH}	Δ_{ZZH}	Δ_{ttH}	Δ_{bbH}	$\Delta_{\tau\tau H}$	$\Delta_{\gamma\gamma H}$	Δ_{ggH}	m_H
true	-0.13	-0.13	-0.19	3.27	3.29	0.19	-0.28	120.0
errors	± 0.45	± 0.61	± 0.63	± 2.34	± 3.35	± 0.99	± 1.12	± 0.29
	-0.43	-0.99	-0.60	-3.68	-3.23	-0.70	-0.69	-0.29
	+0.48	+0.52	+0.65	+1.52	+3.58	+1.30	+1.46	+0.30

Table 4.13: True couplings for the SPS1a-inspired scenario. The errors were calculated for 30 fb^{-1} with 10000 toy experiments (taken from [36]).

The datasets were modified to take into account the modification of the couplings. With respect to SPS1a, $\tan\beta$ was modified to 7, A_t to $-1100 \text{ GeV}/c^2$ and m_A to $151 \text{ GeV}/c^2$. The true values for all Higgs couplings are listed in the first line of Table 4.13. Comparing these deviations with the Standard Model error bands in Table 4.11, it seems daunting to draw conclusions from the individual measurements, but in addition to the individual precision of the coupling measurements, the full correlation matrix (added information) is used.

The first question to be asked is whether the Standard Model is excluded. The exclusion limit for the Standard Model is calculated by determining the χ^2 distribution for smeared Standard Model datasets, calculated with the fixed Standard Model couplings. The integral over χ^2 to 90% of the datasets gives the 90% confidence level. Then the new physics (SPS1a-modified) datasets are used and the χ^2 is calculated with the Standard Model couplings. The two dimensional results are that for 77% of the toy experiments the Standard Model is excluded at a confidence level of 90%. A discovery is much more difficult, for 4% of the toy experiments the new physics scenario is a better description of the datasets than the Standard Model. Using the Higgs coupling measurements, one may be able to exclude the Standard Model, but a discovery will be difficult.

Chapter 5

Conclusions

After many years of preparation, the LHC has started operations in 2008. The first collisions are expected in the run 2009/2010 which will start in November 2009. The increase of the center-of-mass energy beyond the TeVatron will open up a new energy regime to search for new physics.

The first year(s) of LHC and ATLAS/CMS operations will concentrate on the understanding of the detector using Standard Model processes such as the production and decay of the Z boson and lower mass resonances such as the J/ψ . An essential step for the discovery of new physics will be to prove and improve the understanding of the Standard Model at the LHC.

Once the detectors and the backgrounds are understood, the search for new physics, the Higgs boson, supersymmetry and others (extra dimensions) will commence. If supersymmetry is at low mass as hinted by electroweak precision data, large signals are expected and many observables will be measured.

Disentangling the fundamental parameters from the measurements necessitates powerful tools such as SFitter and Fittino as observables depend on different combinations of them. Additionally, the parameter space has large dimensions, thus efficient ways of sampling are needed.

The project SFitter has developed a framework for such an endeavor. Tools such as weighted Markov chains have been developed to sample the parameter space. Interfaces to the most precise theoretical predictions of observables have been built. A rigorous treatment of statistical, systematic and theoretical errors, correlated or not, is provided.

Using SFitter, two projects have been described here. The Higgs sector was studied in the Standard Model as well as in supersymmetry, using

only the expected measurements for a low mass Higgs. The supersymmetric parameters have been studied at the electroweak scale in the MSSM. The parameters have also been studied at the GUT scale in a top-down approach (mSUGRA).

In addition to these studies, SFitter has also analyzed the impact of $(g-2)_\mu$ on the precision of the determination of supersymmetric parameters in a Les Houches project [196]. In [197] the LHC potential for the parameter determination of Split-Supersymmetry was studied. New SFitter projects are already on the way. From one, excerpts were already shown in this paper: a study of the extrapolation of the supersymmetric parameters from the electroweak scale to the high scale. Another study will be the implication of the supersymmetric parameter determination at the LHC on the prediction of the relic density. Here we also plan to include direct/indirect detection results.

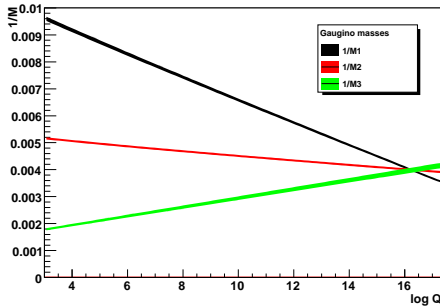


Figure 5.1: Extrapolation of the gaugino mass parameters from the electroweak scale to the GUT scale using LHC and ILC measurements.

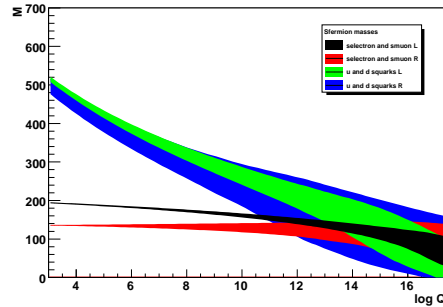


Figure 5.2: Extrapolation of the scalar mass parameters from the electroweak scale to the GUT scale using LHC and ILC measurements.

The tools developed by SFitter can also be used for other models where it is difficult to disentangle for the measurements the fundamental parameters. Nature be supersymmetric or not, with the LHC/ATLAS now and an ILC in the future, particle physics will continue to provide exciting measurements and insights into nature. Maybe SFitter will take us, supersymmetry existing, with the LHC and ILC to the GUT scale, close to the Planck scale, as shown in Figures 5.1 for the gaugino mass parameters and in Figure 5.2 for the scalar mass parameters of the first and second generation.

Bibliography

- [1] S. L. Glashow, Nucl. Phys. **22** (1961) 579.
- [2] A. Salam, *Originally printed in *Svartholm: Elementary Particle Theory, Proceedings Of The Nobel Symposium Held 1968 At Lerum, Sweden*, Stockholm 1968, 367-377*
- [3] S. Weinberg, Phys. Rev. Lett. **19**, 1264 (1967).
- [4] P. W. Higgs, Phys. Lett. **12**, 132 (1964).
- [5] P. W. Higgs, Phys. Rev. **145**, 1156 (1966).
- [6] P. W. Higgs, Phys. Rev. Lett. **13**, 508 (1964).
- [7] F. Englert and R. Brout, Phys. Rev. Lett. **13**, 321 (1964).
- [8] G. S. Guralnik, C. R. Hagen and T. W. B. Kibble, Phys. Rev. Lett. **13**, 585 (1964).
- [9] J. Wess, arXiv:0902.2201 [hep-th].
- [10] Yu. A. Golfand and E. P. Likhtman, JETP Lett. **13** (1971) 323 [Pisma Zh. Eksp. Teor. Fiz. **13** (1971) 452].
- [11] D. V. Volkov and V. P. Akulov, Phys. Lett. B **46**, 109 (1973).
- [12] J. Wess and B. Zumino, Nucl. Phys. B **70**, 39 (1974).
- [13] P. Fayet and J. Iliopoulos, Phys. Lett. B **51**, 461 (1974).
- [14] S. P. Martin, arXiv:hep-ph/9709356.
- [15] S. Dawson and H. Georgi, Phys. Rev. Lett. **43**, 821 (1979).

- [16] M. B. Einhorn and D. R. T. Jones, Nucl. Phys. B **196**, 475 (1982).
- [17] U. Amaldi, W. de Boer and H. Furstenau, Phys. Lett. B **260**, 447 (1991).
- [18] R. Barate *et al.* [LEP Working Group for Higgs boson searches and ALEPH Collaboration and and], Phys. Lett. B **565** (2003) 61 [arXiv:hep-ex/0306033].
- [19] G. Bernardi *et al.* [Tevatron New Phenomena Higgs Working Group and CDF Collaboration and D], arXiv:0808.0534 [hep-ex].
- [20] G. Bernardi *et al.* [Tevatron New Phenomena Higgs Working Group and CDF Collaboration and D], *Combined CDF and D0 Upper Limits on Standard Model Higgs Boson Production with up to 4.2 fb⁻¹ of data*, 2008.
- [21] J. Alcaraz *et al.* [LEP Collaborations and ALEPH Collaboration and DELPHI Collaboration an], arXiv:0712.0929 [hep-ex].
- [22] T. Aaltonen *et al.* [CDF Collaboration], Phys. Rev. D **77**, 112001 (2008) [arXiv:0708.3642 [hep-ex]].
- [23] V. M. Abazov *et al.* [D0 Collaboration], arXiv:0908.0766 [hep-ex].
- [24] E. W. Varnes [CDF Collaboration and D0 Collaboration], Int. J. Mod. Phys. A **23**, 4421 (2008) [arXiv:0810.3652 [hep-ex]].
- [25] S. Schael *et al.* [ALEPH Collaboration and DELPHI Collaboration and L3 Collaboration and], Eur. Phys. J. C **47**, 547 (2006) [arXiv:hep-ex/0602042].
- [26] [LEP Higgs Working Group for Higgs boson searches and ALEPH Collaboration an], arXiv:hep-ex/0107031.
- [27] [LEP SUSY Working Group], *Combined LEP Selectron/Smuon/Stau Results, 183–208 GeV*, 2001, [arXiv:hep-ex/0107031].
- [28] [LEP SUSY Working Group], *Combined LEP Chargino Results up to 208 GeV for large m₀*, 2001, [arXiv:hep-ex/0107031].
- [29] [LEP SUSY Working Group], *Interpretation of the results in mSUGRA*, 2002, [arXiv:hep-ex/0107031].

- [30] J. F. Grivaz, *Int. J. Mod. Phys. A* **23**, 3849 (2008) [arXiv:0809.0531 [hep-ex]].
- [31] G. Aad *et al.* [The ATLAS Collaboration], arXiv:0901.0512 [hep-ex].
- [32] D. Zerwas [ATLAS Collaboration], “First Physics With Atlas,” ATLAS-PROC-2009-015.
- [33] N. J. Buchanan *et al.*, *JINST* **3**, P03004 (2008).
- [34] R. Lafaye, T. Plehn and D. Zerwas, arXiv:hep-ph/0404282.
- [35] R. Lafaye, T. Plehn, M. Rauch and D. Zerwas, *Eur. Phys. J. C* **54**, 617 (2008) [arXiv:0709.3985 [hep-ph]].
- [36] R. Lafaye, T. Plehn, M. Rauch, D. Zerwas and M. Duhrssen, *JHEP*0908 (2009) 009, [arXiv:0904.3866 [hep-ph]].
- [37] U. Ellwanger, arXiv:0908.4231 [hep-ph].
- [38] R. Haag, J. T. Lopuszanski and M. Sohnius, *Nucl. Phys. B* **88**, 257 (1975).
- [39] S. R. Coleman and J. Mandula, *Phys. Rev.* **159**, 1251 (1967).
- [40] L. Girardello and M. T. Grisaru, *Nucl. Phys. B* **194**, 65 (1982).
- [41] H. E. Haber and G. L. Kane, *Phys. Rept.* **117**, 75 (1985).
- [42] G. R. Farrar and P. Fayet, *Phys. Lett. B* **76**, 575 (1978).
- [43] J. A. Aguilar-Saavedra *et al.*, *Eur. Phys. J. C* **46**, 43 (2006) [arXiv:hep-ph/0511344].
- [44] L. E. Ibanez and G. G. Ross, arXiv:hep-ph/9204201.
- [45] B. C. Allanach *et al.*, in *Proc. of the APS/DPF/DPB Summer Study on the Future of Particle Physics (Snowmass 2001)* ed. N. Graf, *Eur. Phys. J. C* **25**, 113 (2002) [arXiv:hep-ph/0202233].
- [46] G. Weiglein *et al.* [LHC/LC Study Group], *Phys. Rept.* **426**, 47 (2006) [arXiv:hep-ph/0410364].

- [47] G. L. Bayatian *et al.* [CMS Collaboration], *J. Phys. G* **34**, 995 (2007).
- [48] L. Evans and P. Bryant, *JINST* **3** (2008) S08001.
- [49] G. Aad *et al.* [ATLAS Collaboration], *JINST* **3**, S08003 (2008).
- [50] M. Aharrouche *et al.*, *Nucl. Instrum. Meth. A* **597**, 178 (2008).
- [51] J. Colas *et al.*, *Nucl. Instrum. Meth. A* **582**, 429 (2007) [arXiv:0709.1094 [physics.ins-det]].
- [52] M. Aharrouche *et al.* [ATLAS Electromagnetic Barrel Calorimeter Collaboration], *Nucl. Instrum. Meth. A* **568**, 601 (2006) [arXiv:physics/0608012].
- [53] B. Aubert *et al.* [ATLAS Electromagnetic Barrel Liquid Argon Calorimeter Group], *Nucl. Instrum. Meth. A* **558**, 388 (2006).
- [54] J. Colas *et al.* [ATLAS Liquid Argon Calorimeter Collaboration], *Nucl. Instrum. Meth. A* **550**, 96 (2005) [arXiv:physics/0505127].
- [55] B. Aubert *et al.* [The ATLAS Electromagnetic Liquid Argon Calorimeter Group], *Nucl. Instrum. Meth. A* **500**, 178 (2003).
- [56] B. Aubert *et al.* [ATLAS Electromagnetic Liquid Argon Calorimeter Group], *Nucl. Instrum. Meth. A* **500**, 202 (2003) [Erratum-ibid. A **517**, 399 (2004)].
- [57] J. Brau *et al.*, “International Linear Collider reference design report. 1: Executive summary. 2: Physics at the ILC. 3: Accelerator. 4: Detectors,”
- [58] ILD concept group, *The International Large Detector, Letter of Intent* (2009).
- [59] SiD, *Letter of Intent* (2009).
- [60] M. . Battaglia, A. De Roeck, J. R. Ellis and D. Schulte, “Physics at the CLIC multi-TeV linear collider: Report of the CLIC Physics Working Group”.
- [61] B. C. Allanach, *Eur. Phys. J. C* **59** (2009) 427 [arXiv:0805.2088 [hep-ph]].

- [62] A. Djouadi, J. L. Kneur and G. Moultaka, *Comput. Phys. Commun.* **176**, 426 (2007) [arXiv:hep-ph/0211331].
- [63] B. C. Allanach, *Comput. Phys. Commun.* **143**, 305 (2002) [arXiv:hep-ph/0104145].
- [64] W. Porod, *Comput. Phys. Commun.* **153**, 275 (2003) [arXiv:hep-ph/0301101].
- [65] M. Muhlleitner, A. Djouadi and Y. Mambrini, *Comput. Phys. Commun.* **168**, 46 (2005) [arXiv:hep-ph/0311167].
- [66] A. Djouadi, M. M. Muhlleitner and M. Spira, *Acta Phys. Polon. B* **38**, 635 (2007) [arXiv:hep-ph/0609292].
- [67] A. Djouadi, J. Kalinowski and M. Spira, *Comput. Phys. Commun.* **108**, 56 (1998) [arXiv:hep-ph/9704448].
- [68] T. Sjostrand, S. Mrenna and P. Skands, *JHEP* **0605**, 026 (2006) [arXiv:hep-ph/0603175].
- [69] W. Beenakker, R. Hopker, M. Spira and P. M. Zerwas, *Nucl. Phys. B* **492**, 51 (1997) [arXiv:hep-ph/9610490].
- [70] W. Beenakker, M. Kramer, T. Plehn, M. Spira and P. M. Zerwas, *Nucl. Phys. B* **515**, 3 (1998) [arXiv:hep-ph/9710451].
- [71] W. Beenakker, M. Klasen, M. Kramer, T. Plehn, M. Spira and P. M. Zerwas, *Phys. Rev. Lett.* **83**, 3780 (1999) [Erratum-ibid. **100**, 029901 (2008)] [arXiv:hep-ph/9906298].
- [72] T. Plehn, arXiv:hep-ph/9809319.
- [73] G. A. Blair, W. Porod and P. M. Zerwas, *Eur. Phys. J. C* **27**, 263 (2003) [arXiv:hep-ph/0210058].
- [74] B. C. Allanach, G. A. Blair, S. Kraml, H. U. Martyn, G. Polesello, W. Porod and P. M. Zerwas, arXiv:hep-ph/0403133.
- [75] P. Bechtle, K. Desch, W. Porod and P. Wienemann, *Eur. Phys. J. C* **46**, 533 (2006) [arXiv:hep-ph/0511006].

- [76] R. R. de Austri, R. Trotta and L. Roszkowski, JHEP **0605**, 002 (2006) [arXiv:hep-ph/0602028].
- [77] D. N. Spergel *et al.* [WMAP Collaboration], Astrophys. J. Suppl. **170**, 377 (2007) [arXiv:astro-ph/0603449].
- [78] M. Davier, A. Hoecker, B. Malaescu, C. Z. Yuan and Z. Zhang, arXiv:0908.4300 [hep-ph].
- [79] O. Buchmueller *et al.*, Phys. Lett. B **657**, 87 (2007) [arXiv:0707.3447 [hep-ph]].
- [80] P. Bechtle, K. Desch, M. Uhlenbrock and P. Wienemann, arXiv:0907.2589 [hep-ph].
- [81] O. Buchmueller *et al.*, JHEP **0809** (2008) 117 [arXiv:0808.4128 [hep-ph]].
- [82] S. S. AbdusSalam, B. C. Allanach, F. Quevedo, F. Feroz and M. Hobson, arXiv:0904.2548 [hep-ph].
- [83] S. Dawson, E. Eichten and C. Quigg, Phys. Rev. D **31**, 1581 (1985).
- [84] B. C. Allanach, K. Cranmer, C. G. Lester and A. M. Weber, JHEP **0708**, 023 (2007) [arXiv:0705.0487 [hep-ph]].
- [85] H. M. Georgi, S. L. Glashow, M. E. Machacek and D. V. Nanopoulos, Phys. Rev. Lett. **40**, 692 (1978).
- [86] M. Duehrssen, *Prospects for the measurement of Higgs boson coupling parameters in the mass range from 110 - 190 GeV/c²*, (2003), ATL-PHYS-2003-030.
- [87] J. M. Butterworth, A. R. Davison, M. Rubin and G. P. Salam, Phys. Rev. Lett. **100**, 242001 (2008) [arXiv:0802.2470 [hep-ph]].
- [88] ATLAS Collaboration, ATL-PHYS-PUB-2009-088.
- [89] M. Spira, arXiv:hep-ph/9510347.
- [90] A. Freitas, A. von Manteuffel and P. M. Zerwas, Eur. Phys. J. C **34**, 487 (2004) [arXiv:hep-ph/0310182].

- [91] D. M. Pierce, J. A. Bagger, K. T. Matchev and R. j. Zhang, Nucl. Phys. B **491**, 3 (1997) [arXiv:hep-ph/9606211].
- [92] T. Fritzsche and W. Hollik, Nucl. Phys. Proc. Suppl. **135**, 102 (2004) [arXiv:hep-ph/0407095].
- [93] W. Oller, H. Eberl and W. Majerotto, Phys. Lett. B **590**, 273 (2004) [arXiv:hep-ph/0402134].
- [94] A. Hocker, H. Lacker, S. Laplace and F. Le Diberder, Eur. Phys. J. C **21**, 225 (2001) [arXiv:hep-ph/0104062].
- [95] J. Charles, A. Hocker, H. Lacker, F. R. Le Diberder and S. T'Jampens, arXiv:hep-ph/0607246.
- [96] B. C. Allanach and C. G. Lester, Phys. Rev. D **73**, 015013 (2006) [arXiv:hep-ph/0507283].
- [97] B. C. Allanach and C. G. Lester, Comput. Phys. Commun. **179**, 256 (2008) [arXiv:0705.0486 [hep-ph]].
- [98] B. C. Allanach, Phys. Lett. B **635**, 123 (2006) [arXiv:hep-ph/0601089].
- [99] H. E. Haber, R. Hempfling and A. H. Hoang, Z. Phys. C **75**, 539 (1997) [arXiv:hep-ph/9609331].
- [100] G. Degrossi, S. Heinemeyer, W. Hollik, P. Slavich and G. Weiglein, Eur. Phys. J. C **28**, 133 (2003) [arXiv:hep-ph/0212020].
- [101] M. Frank, T. Hahn, S. Heinemeyer, W. Hollik, H. Rzehak and G. Weiglein, JHEP **0702**, 047 (2007) [arXiv:hep-ph/0611326].
- [102] C. A. Nelson, Phys. Rev. D **37**, 1220 (1988).
- [103] M. Dittmar and H. K. Dreiner, Phys. Rev. D **55**, 167 (1997) [arXiv:hep-ph/9608317].
- [104] C. Anastasiou, G. Dissertori, F. Stockli and B. R. Webber, JHEP **0803**, 017 (2008) [arXiv:0801.2682 [hep-ph]].
- [105] M. Grazzini, JHEP **0802**, 043 (2008) [arXiv:0801.3232 [hep-ph]].

- [106] H. Bachacou, I. Hinchliffe and F. E. Paige, Phys. Rev. D **62**, 015009 (2000) [arXiv:hep-ph/9907518].
- [107] B. C. Allanach, C. G. Lester, M. A. Parker and B. R. Webber, JHEP **0009**, 004 (2000) [arXiv:hep-ph/0007009].
- [108] B. K. Gjelsten, D. J. . Miller and P. Osland, JHEP **0506**, 015 (2005) [arXiv:hep-ph/0501033].
- [109] B. K. Gjelsten, D. J. . Miller and P. Osland, JHEP **0412**, 003 (2004) [arXiv:hep-ph/0410303].
- [110] A. H. Hoang, arXiv:hep-ph/0412160.
- [111] P. M. Ferreira, I. Jack and D. R. T. Jones, Phys. Lett. B **387**, 80 (1996) [arXiv:hep-ph/9605440].
- [112] B. C. Allanach, S. Kraml and W. Porod, JHEP **0303**, 016 (2003) [arXiv:hep-ph/0302102].
- [113] I. Jack, D. R. T. Jones and A. F. Kord, Annals Phys. **316**, 213 (2005) [arXiv:hep-ph/0408128].
- [114] M. Drees and S. P. Martin, arXiv:hep-ph/9504324.
- [115] V. D. Barger, T. Falk, T. Han, J. Jiang, T. Li and T. Plehn, Phys. Rev. D **64**, 056007 (2001) [arXiv:hep-ph/0101106].
- [116] V. D. Barger, T. Han, T. J. Li and T. Plehn, Phys. Lett. B **475**, 342 (2000) [arXiv:hep-ph/9907425].
- [117] L. J. Hall, V. A. Kostelecky and S. Raby, Nucl. Phys. B **267**, 415 (1986).
- [118] G. D'Ambrosio, G. F. Giudice, G. Isidori and A. Strumia, Nucl. Phys. B **645**, 155 (2002) [arXiv:hep-ph/0207036].
- [119] S. Dittmaier, G. Hiller, T. Plehn and M. Spannowsky, Phys. Rev. D **77**, 115001 (2008) [arXiv:0708.0940 [hep-ph]].
- [120] J. Hisano, K. Kawagoe and M. M. Nojiri, Phys. Rev. D **68**, 035007 (2003) [arXiv:hep-ph/0304214].

- [121] T. Goto, K. Kawagoe and M. M. Nojiri, Phys. Rev. D **70**, 075016 (2004) [Erratum-ibid. D **71**, 059902 (2005)] [arXiv:hep-ph/0406317].
- [122] J. R. Ellis, S. Heinemeyer, K. A. Olive, A. M. Weber and G. Weiglein, JHEP **0708**, 083 (2007) [arXiv:0706.0652 [hep-ph]].
- [123] L. Roszkowski, R. R. de Austri, J. Silk and R. Trotta, Phys. Lett. B **671**, 10 (2009) [arXiv:0707.0622 [astro-ph]].
- [124] R. Trotta, R. Ruiz de Austri and L. Roszkowski, J. Phys. Conf. Ser. **60**, 259 (2007).
- [125] R. Trotta, R. R. de Austri and L. Roszkowski, New Astron. Rev. **51**, 316 (2007) [arXiv:astro-ph/0609126].
- [126] J. R. Ellis, K. A. Olive, Y. Santoso and V. C. Spanos, Phys. Lett. B **603**, 51 (2004) [arXiv:hep-ph/0408118].
- [127] J. R. Ellis, K. A. Olive, Y. Santoso and V. C. Spanos, Phys. Rev. D **69**, 095004 (2004) [arXiv:hep-ph/0310356].
- [128] E. A. Baltz, M. Battaglia, M. E. Peskin and T. Wizansky, Phys. Rev. D **74**, 103521 (2006) [arXiv:hep-ph/0602187].
- [129] J. L. Kneur and N. Sahoury, arXiv:0808.0144 [hep-ph].
- [130] M. Spira, A. Djouadi, D. Graudenz and P. M. Zerwas, Nucl. Phys. B **453**, 17 (1995) [arXiv:hep-ph/9504378].
- [131] M. Spira, Fortsch. Phys. **46**, 203 (1998) [arXiv:hep-ph/9705337].
- [132] R. V. Harlander and W. B. Kilgore, Phys. Rev. Lett. **88**, 201801 (2002) [arXiv:hep-ph/0201206].
- [133] C. Anastasiou and K. Melnikov, Nucl. Phys. B **646**, 220 (2002) [arXiv:hep-ph/0207004].
- [134] C. Anastasiou, R. Boughezal and F. Petriello, JHEP **0904** (2009) 003 [arXiv:0811.3458 [hep-ph]].
- [135] V. Ravindran, J. Smith and W. L. van Neerven, Nucl. Phys. B **665**, 325 (2003) [arXiv:hep-ph/0302135].

- [136] C. Anastasiou, K. Melnikov and F. Petriello, Phys. Rev. D **72**, 097302 (2005) [arXiv:hep-ph/0509014].
- [137] C. Anastasiou, L. J. Dixon, K. Melnikov and F. Petriello, Phys. Rev. D **69**, 094008 (2004) [arXiv:hep-ph/0312266].
- [138] S. Catani and M. Grazzini, Phys. Rev. Lett. **98**, 222002 (2007) [arXiv:hep-ph/0703012].
- [139] S. Catani, D. de Florian, M. Grazzini and P. Nason, JHEP **0307**, 028 (2003) [arXiv:hep-ph/0306211].
- [140] G. Bozzi, S. Catani, D. de Florian and M. Grazzini, Nucl. Phys. B **737**, 73 (2006) [arXiv:hep-ph/0508068].
- [141] D. L. Rainwater, D. Zeppenfeld and K. Hagiwara, Phys. Rev. D **59**, 014037 (1999) [arXiv:hep-ph/9808468].
- [142] T. Plehn, D. L. Rainwater and D. Zeppenfeld, Phys. Rev. D **61**, 093005 (2000) [arXiv:hep-ph/9911385].
- [143] D. L. Rainwater and D. Zeppenfeld, Phys. Rev. D **60**, 113004 (1999) [Erratum-ibid. D **61**, 099901 (2000)] [arXiv:hep-ph/9906218].
- [144] N. Kauer, T. Plehn, D. L. Rainwater and D. Zeppenfeld, Phys. Lett. B **503**, 113 (2001) [arXiv:hep-ph/0012351].
- [145] V. D. Barger, R. J. N. Phillips and D. Zeppenfeld, Phys. Lett. B **346**, 106 (1995) [arXiv:hep-ph/9412276].
- [146] D. L. Rainwater, R. Szalapski and D. Zeppenfeld, Phys. Rev. D **54**, 6680 (1996) [arXiv:hep-ph/9605444].
- [147] V. Del Duca *et al.*, JHEP **0610**, 016 (2006) [arXiv:hep-ph/0608158].
- [148] T. Han, G. Valencia and S. Willenbrock, Phys. Rev. Lett. **69**, 3274 (1992) [arXiv:hep-ph/9206246].
- [149] T. Figy, C. Oleari and D. Zeppenfeld, Phys. Rev. D **68**, 073005 (2003) [arXiv:hep-ph/0306109].
- [150] M. Ciccolini, A. Denner and S. Dittmaier, Phys. Rev. Lett. **99**, 161803 (2007) [arXiv:0707.0381 [hep-ph]].

- [151] M. Ciccolini, A. Denner and S. Dittmaier, Phys. Rev. D **77**, 013002 (2008) [arXiv:0710.4749 [hep-ph]].
- [152] K. Arnold *et al.*, Comput. Phys. Commun. **180**, 1661 (2009) [arXiv:0811.4559 [hep-ph]].
- [153] J. R. Andersen, T. Binoth, G. Heinrich and J. M. Smillie, JHEP **0802**, 057 (2008) [arXiv:0709.3513 [hep-ph]].
- [154] A. Bredenstein, K. Hagiwara and B. Jager, Phys. Rev. D **77**, 073004 (2008) [arXiv:0801.4231 [hep-ph]].
- [155] K. Cranmer, Y. Q. Fang, B. Mellado, S. Paganis, W. Quayle and S. L. Wu, arXiv:hep-ph/0401148.
- [156] J. R. Forshaw and M. Sjordahl, JHEP **0709**, 119 (2007) [arXiv:0705.1504 [hep-ph]].
- [157] J. R. Andersen, V. Del Duca and C. D. White, JHEP **0902**, 015 (2009) [arXiv:0808.3696 [hep-ph]].
- [158] V. Del Duca, W. Kilgore, C. Oleari, C. Schmidt and D. Zeppenfeld, Phys. Rev. Lett. **87**, 122001 (2001) [arXiv:hep-ph/0105129].
- [159] A. Nikitenko and M. Vazquez Acosta, arXiv:0705.3585 [hep-ph].
- [160] W. Beenakker, S. Dittmaier, M. Kramer, B. Plumper, M. Spira and P. M. Zerwas, Phys. Rev. Lett. **87**, 201805 (2001) [arXiv:hep-ph/0107081].
- [161] W. Beenakker, S. Dittmaier, M. Kramer, B. Plumper, M. Spira and P. M. Zerwas, Nucl. Phys. B **653**, 151 (2003) [arXiv:hep-ph/0211352].
- [162] S. Dawson, L. H. Orr, L. Reina and D. Wackerroth, Phys. Rev. D **67**, 071503 (2003) [arXiv:hep-ph/0211438].
- [163] D. A. Dicus, C. Kao and S. S. D. Willenbrock, Phys. Lett. B **203**, 457 (1988).
- [164] E. W. N. Glover and J. J. van der Bij, Nucl. Phys. B **309**, 282 (1988).
- [165] T. Plehn, M. Spira and P. M. Zerwas, Nucl. Phys. B **479**, 46 (1996) [Erratum-ibid. B **531**, 655 (1998)] [arXiv:hep-ph/9603205].

- [166] A. Djouadi, W. Kilian, M. Muhlleitner and P. M. Zerwas, Eur. Phys. J. C **10**, 45 (1999) [arXiv:hep-ph/9904287].
- [167] S. Dawson, S. Dittmaier and M. Spira, Phys. Rev. D **58**, 115012 (1998) [arXiv:hep-ph/9805244].
- [168] U. Baur, T. Plehn and D. L. Rainwater, Phys. Rev. D **67**, 033003 (2003) [arXiv:hep-ph/0211224].
- [169] U. Baur, T. Plehn and D. L. Rainwater, Phys. Rev. Lett. **89**, 151801 (2002) [arXiv:hep-ph/0206024].
- [170] A. Dahlhoff, arXiv:hep-ex/0505022.
- [171] U. Baur, T. Plehn and D. L. Rainwater, Phys. Rev. D **69**, 053004 (2004) [arXiv:hep-ph/0310056].
- [172] G. Cacciapaglia, A. Deandrea and J. Llodra-Perez, JHEP **0906**, 054 (2009) [arXiv:0901.0927 [hep-ph]].
- [173] V. Barger, T. Han, P. Langacker, B. McElrath and P. Zerwas, Phys. Rev. D **67**, 115001 (2003) [arXiv:hep-ph/0301097].
- [174] C. Grojean, G. Servant and J. D. Wells, Phys. Rev. D **71**, 036001 (2005) [arXiv:hep-ph/0407019].
- [175] S. Kanemura, Y. Okada, E. Senaha and C. P. Yuan, Phys. Rev. D **70**, 115002 (2004) [arXiv:hep-ph/0408364].
- [176] J. R. Dell'Aquila and C. A. Nelson, Phys. Rev. D **33**, 93 (1986).
- [177] T. Plehn, D. L. Rainwater and D. Zeppenfeld, Phys. Rev. Lett. **88**, 051801 (2002) [arXiv:hep-ph/0105325].
- [178] C. P. Buszello, I. Fleck, P. Marquard and J. J. van der Bij, Eur. Phys. J. C **32**, 209 (2004) [arXiv:hep-ph/0212396].
- [179] V. Hankele, G. Klamke, D. Zeppenfeld and T. Figy, Phys. Rev. D **74**, 095001 (2006) [arXiv:hep-ph/0609075].
- [180] C. Ruwiedel, N. Wermes and M. Schumacher, Eur. Phys. J. C **51**, 385 (2007).

- [181] E. A. Baltz and P. Gondolo, JHEP **0410**, 052 (2004) [arXiv:hep-ph/0407039].
- [182] T. Plehn, D. L. Rainwater and D. Zeppenfeld, Phys. Lett. B **454**, 297 (1999) [arXiv:hep-ph/9902434].
- [183] M. Schumacher, arXiv:hep-ph/0410112.
- [184] W. Hollik, T. Plehn, M. Rauch and H. Rzehak, Phys. Rev. Lett. **102**, 091802 (2009) [arXiv:0804.2676 [hep-ph]].
- [185] U. Ellwanger, J. F. Gunion and C. Hugonie, JHEP **0507**, 041 (2005) [arXiv:hep-ph/0503203].
- [186] A. Martin, arXiv:hep-ph/0703247.
- [187] M. Carena, T. Han, G. Y. Huang and C. E. M. Wagner, JHEP **0804**, 092 (2008) [arXiv:0712.2466 [hep-ph]].
- [188] S. Chang, R. Dermisek, J. F. Gunion and N. Weiner, Ann. Rev. Nucl. Part. Sci. **58**, 75 (2008) [arXiv:0801.4554 [hep-ph]].
- [189] S. Chang and T. Gregoire, arXiv:0903.0403 [hep-ph].
- [190] A. Alves, O. Eboli, T. Plehn and D. L. Rainwater, Phys. Rev. D **69**, 075005 (2004) [arXiv:hep-ph/0309042].
- [191] D. Zeppenfeld, R. Kinnunen, A. Nikitenko and E. Richter-Was, Phys. Rev. D **62**, 013009 (2000) [arXiv:hep-ph/0002036].
- [192] M. Duhrssen, S. Heinemeyer, H. Logan, D. Rainwater, G. Weiglein and D. Zeppenfeld, arXiv:hep-ph/0407190.
- [193] R. V. Harlander and M. Steinhauser, Phys. Lett. B **574**, 258 (2003) [arXiv:hep-ph/0307346].
- [194] R. V. Harlander and M. Steinhauser, JHEP **0409**, 066 (2004) [arXiv:hep-ph/0409010].
- [195] C. Anastasiou, S. Beerli and A. Daleo, Phys. Rev. Lett. **100**, 241806 (2008) [arXiv:0803.3065 [hep-ph]].
- [196] M. M. Nojiri *et al.*, arXiv:0802.3672 [hep-ph].

- [197] E. Turlay, “Supersymétrie avec scalaires découplés et reconstruction et identification des électrons dans le détecteur ATLAS”, LAL-09-37.

Acknowledgements

Pierre Binétruy m'a appelé en decembre 2002 pour me demander si je voulais bien m'occuper d'un groupe dans le GDR Supersymétrie. Cet appel a in fine donné naissance à SFitter. Je voudrais donc remercier les SFitter: Rémi Lafaye, Tilman Plehn et Michael Rauch pour le travail en commun décrit partiellement dans ce manuscrit. J'ai beaucoup apprécié de travailler avec Jean-Loic Kneur, Michael Dührssen et Claire Adam sur des projets SFitter.

Je suis encore surpris qu'on m'ait laissé toucher l'électronique d'ATLAS. Une amie de longue date a remarqué: "Tu fais des études de physique, mais tu es incapable de réparer une prise électrique." Le travail sur des FEBs, stressant et intéressant, a été l'effort de toute une équipe. Merci à Dominique Breton le magicien de l'électronique, Isabelle Falleau et Antoine Pérus qui ont fait des miracles pour écrire et faire fonctionner le soft. Sans le travail efficace (qui n'a pas été facile) de Patrick Favre, Alain Bozone, Stéphane Trochet, Olivier Bohner, Michèle Quentin, Bernard de Bennerot, Matthieu Lechowski ainsi que plusieurs étudiants/stagiaires nous n'aurions jamais pu tenir les delais. Pierre Imbert s'est dévoué pour faire la navette entre le réparateur et l'équipe afin d'accélérer. L'équipe de transport du LAL a démontré qu'il faut éviter de sous-traiter...(vous connaissez GEFCO?)

Coté software et egamma, je remercie David Rousseau et Srimi Rajagopalan pour avoir guidé mes pas et leur support quand je coordonnais ATLAS-egamma. Merci à Fred Derue pour sa contribution permanente et stable à egamma. J'ai appris beaucoup de Daniel Froidevaux qui a du souffrir avec une personne aussi bavarde que moi.

Un grand merci à Geneviève Gilbert et aux membres du service mission et des services administratives du LAL pour leur aide quotidien et leur support dans la gestion du GDR Terascale.

Je remercie les rapporteurs, Sally Dawson, (Fittino) Klaus Desch et Horst Oberlack, mon chef quand j'étais coordinateur egamma, de m'avoir fait l'honneur de venir. Je remercie chaleureusement Jean Orloff, mon chef en tant que directeur du GDR Supersymétrie pendant quatre ans, Guy Wormser, directeur du LAL et Daniel Fournier, mon chef du groupe ATLAS pendant 11 ans et père du calorimètre électromagnétique d'ATLAS, d'avoir accepté de faire partie du jury.

Des remerciements ne seraient pas complets sans remercier les membres du groupe ATLAS, Laurent, mon chef lors du test beam pendant des années pour de nombreux conseils, Louis, Lydia, David, Marumi, RD, Jean-Baptiste,

Caroline et beaucoup d'autres. J'ai particulièrement apprécié de travailler avec Emmanuel Turlay, Andrea Thamm, Adrien Renaud.

Je voudrais remercier le conseil scientifique de l'Université Paris-Sud pour sa contribution à mon repertoire d'anecdotes.

Finalement un grand merci à mon père, Christiane, Sophie et Rebecca pour tout!